

Detecting Sunyaev-Zel’dovich clusters with *Planck*: II. Foreground components and optimised filtering schemes

B. M. Schäfer^{1*}, C. Pfrommer^{1*}, R. M. Hell^{1*} and M. Bartelmann^{2*}

¹Max-Planck-Institut für Astrophysik, Karl-Schwarzschild-Straße 1, Postfach 1317, 85741 Garching, Germany

²Institut für theoretische Astrophysik, Tiergartenstraße 15, 69121 Heidelberg, Germany

17 November 2018

ABSTRACT

The *Planck* mission is the most sensitive all-sky CMB experiment currently planned. The High Frequency Instrument (*HFI*) will be especially suited to observe clusters of galaxies by their thermal Sunyaev-Zel’dovich (SZ) effect. In order to assess *Planck*’s SZ-capabilities in the presence of spurious signals, a simulation is presented that combines maps of the thermal and kinetic SZ-effects with a realisation of the cosmic microwave background (CMB), in addition to Galactic foregrounds (synchrotron emission, free-free emission, thermal emission from dust, CO-line radiation) as well as the sub-millimetric emission from celestial bodies of our Solar system. Additionally, observational issues such as the finite angular resolution and spatially non-uniform instrumental noise of *Planck*’s sky maps are taken into account, yielding a set of all-sky flux maps, the auto-correlation and cross-correlation properties of which are examined in detail. In the second part of the paper, filtering schemes based on scale-adaptive and matched filtering are extended to spherical data sets, that enable the amplification of the weak SZ-signal in the presence of all contaminations stated above. The theory of scale-adaptive and matched filtering in the framework of spherical maps is developed, the resulting filter kernel shapes are discussed and their functionality is verified.

Key words: galaxies: clusters: general, cosmology: cosmic microwave background, methods: numerical, space vehicles: *Planck*

1 INTRODUCTION

The Sunyaev-Zel’dovich (SZ) effect (Sunyaev & Zel’dovich 1972, 1980; Rephaeli 1995; Birkinshaw 1999) is the most important extragalactic source of secondary anisotropies in the CMB sky. The thermal SZ-effect is explained by the fact that CMB photons are put in thermal contact with electrons of the hot intra-cluster medium (ICM) by Compton-interactions which causes a transfer of energy from the ICM to the CMB. Because of the smallness of the Thompson cross-section and of the diluteness of the ICM this transfer of thermal energy is small. In the direction of a cluster, low-energetic photons with frequencies below $\nu = 217$ GHz are removed from the line-of-sight. At frequencies above $\nu = 217$ GHz CMB photons are scattered into the line-of-sight, causing a distinct modulation of the CMB surface brightness as a function of observing frequency, which enables the detection of clusters of galaxies in microwave data.

In contrast, in the kinetic effect it is the peculiar motion of a cluster along the line of sight relative to the CMB frame that induces CMB surface brightness fluctuations. The peculiar motion of

the cluster causes the CMB to be anisotropic in the cluster frame. Due to this symmetry breaking of the scattering geometry, photons scattered into the line-of-sight are shifted in frequency, namely to higher frequencies, if the cluster is moving towards the observer.

The *Planck*-mission will be especially suited to detect SZ-clusters due to its sensitivity, its spectroscopic capabilities, sky coverage and spatial resolution. It is expected to yield a cluster catalogue containing $\approx 10^4$ entries. Extensive literature exists on the topic, but so far the influence of foregrounds and details of *Planck*’s instrumentation and data acquisition have not been thoroughly addressed. In this work we aim at modelling the astrophysical and instrumental issues connected to the observation of SZ-clusters as exhaustively as possible: A simulation is presented that combines realistic maps of both SZ-effects with a realisation of the CMB, with four different Galactic foreground components (thermal dust, free-free emission, synchrotron emission and emission from rotational transitions of CO molecules), with maps containing the sub-millimetric emission from planets and asteroids of the Solar system and with instrumental noise. *Planck*’s frequency response and beam shapes are modelled conforming to the present knowledge of *Planck*’s receivers and its optical system. In order to extract the SZ-cluster signal, filtering schemes based on matched and scale-adaptive filtering are extended to spherical data sets.

In contrast to the recent work by Geisbüsch et al. (2004),

* e-mail: spirou@mpa-garching.mpg.de (BMS); pfrommer@mpa-garching.mpg.de (CP); reinhard@mpa-garching.mpg.de (RMH); mbartelmann@ita.uni-heidelberg.de (MB)

our SZ-simulation does not rely on idealised scaling relations and furthermore, takes account of the cluster's morphological variety. The Galactic foregrounds are modelled in concordance with WMAP observations (see Bennett et al. 2003), which constitutes an improvement over the simplifying assumptions made by Geisbüsch et al. In addition, instrumentation issues such as non-isotropic detector noise are properly incorporated into the simulation. The filter scheme employed in the paper by Geisbüsch et al. is the harmonic-space maximum entropy method introduced by Stolyarov et al. (2002) which assumes approximate prior knowledge of the emission component's power spectra. Its computational demand is much higher than matched and scale-adaptive filtering: In fact, the computations presented in this work can be run on a notebook-class computer.

The paper is structured as follows: After a brief recapitulation of the SZ-effect in Sect. 2, the *Planck*-satellite and instrumental issues connected to observation of CMB anisotropies are described in Sect. 3. The foreground emission components are introduced in Sect. 4. The steps in the simulation of flux maps for the various *Planck*-channels are described and their correlation properties are examined in Sect. 5. The theory of matched and scale-adaptive filtering is extended to spherical data sets and the resulting filter kernel shapes are in detail discussed in Sect. 6. A summary in Sect. 7 concludes the paper.

Throughout the paper, the cosmological model assumed is the standard Λ CDM cosmology, which has recently been supported by observations of the WMAP satellite (Spergel et al. 2003). Parameter values have been chosen as $\Omega_M = 0.3$, $\Omega_\Lambda = 0.7$, $H_0 = 100 h \text{ km s}^{-1} \text{ Mpc}^{-1}$ with $h = 0.7$, $\Omega_B = 0.04$, $n_s = 1$ and $\sigma_8 = 0.9$.

2 SUNYAEV-ZEL'DOVICH DEFINITIONS

The Sunyaev-Zel'dovich effects are the most important extragalactic sources of secondary anisotropies in the CMB. Inverse Compton scattering of CMB photons with electrons of the ionised ICM gives rise to these effects and induce surface brightness fluctuations of the CMB sky, either because of the thermal motion of the ICM electrons (thermal SZ-effect) or because of the bulk motion of the cluster itself relative to the comoving CMB-frame along the line-of-sight (kinetic SZ-effect).

The relative change $\Delta T/T$ in thermodynamic CMB temperature at position θ as a function of dimensionless frequency $x = hv/(k_B T_{\text{CMB}})$ due to the thermal SZ-effect is given by:

$$\frac{\Delta T}{T}(\theta) = y(\theta) \left(x \frac{e^x + 1}{e^x - 1} - 4 \right) \quad \text{with} \quad (1)$$

$$y(\theta) = \frac{\sigma_T k_B}{m_e c^2} \int dl n_e(\theta, l) T_e(\theta, l), \quad (2)$$

where the amplitude y of the thermal SZ-effect is commonly known as the thermal Comptonisation parameter, that itself is defined as the line-of-sight integral of the temperature weighted thermal electron density. m_e , c , k_B and σ_T denote electron mass, speed of light, Boltzmann's constant and the Thompson cross section, respectively. The kinetic SZ-effect arises due to the motion of the cluster parallel to the line of sight relative to the CMB-frame:

$$\frac{\Delta T}{T}(\theta) = -w(\theta) \quad \text{with} \quad w(\theta) = \frac{\sigma_T}{c} \int dl n_e(\theta, l) v_r(\theta, l). \quad (3)$$

Here, v_r is the radial component of the cluster's velocity. The convention is such that $v_r < 0$, if the cluster is moving towards the observer. In this case, the CMB temperature is increased. In analogy,

the quantity w is referred to as the kinetic Comptonisation. The SZ-observables are the line-of-sight Comptonisations integrated over the solid angle subtended by the cluster. The quantities \mathcal{Y} and \mathcal{W} are referred to as the integrated thermal and kinetic Comptonisations, respectively:

$$\mathcal{Y} = \int d\Omega y(\theta) = d_A^{-2}(z) \cdot \frac{\sigma_T k_B}{m_e c^2} \int dV n_e T_e \quad (4)$$

$$\mathcal{W} = \int d\Omega w(\theta) = d_A^{-2}(z) \cdot \frac{\sigma_T}{c} \int dV n_e v_r \quad (5)$$

Here, $d_A(z)$ denotes the angular diameter distance of a cluster situated at redshift z .

3 SUBMILLIMETRIC OBSERVATIONS WITH *Planck*

The *Planck*-mission^{1,2} will perform a polarisation sensitive survey of the complete microwave sky in nine observing frequencies from the Lagrange point L_2 in the Sun-Earth system. It will observe at angular resolutions of up to 5'0 in the best channels and will achieve micro-Kelvin sensitivity relying on bolometric receivers (high frequency instrument *HFI*, described in Lamarre et al. 2003) and on high electron mobility transistors (low frequency instrument *LFI*, see Villa et al. 2003; Bersanelli & Mandolesi 2000). The main characteristics are summarised in Table 1. *Planck*'s beam characteristics are given Sect. 3.1 and the scanning strategy and the simulation of spatially non-uniform detector noise is outlined in Sect. 3.2.

3.1 Beam shapes

The beam shapes of *Planck* are well described by azimuthally symmetric Gaussians $b(\theta) = \frac{1}{2\pi\sigma_\theta^2} \exp\left(-\frac{\theta^2}{2\sigma_\theta^2}\right)$ with $\sigma_\theta = \frac{\Delta\theta}{\sqrt{8 \ln(2)}}$. The residuals from the ideal Gaussian shape (ellipticity, higher order distortions, diffraction rings, far-side lobes, pick-up of stray-light) are expected not to exceed the percent level and are neglected for the purpose of this work. Table 1 gives the angular resolution $\Delta\theta$ in terms of FWHM of each *Planck*-channel for reference.

3.2 Scanning strategy and noise-equivalent maps

CMB observations by *Planck* will proceed in great circles fixed on the ecliptic poles. A single scan will start at the North ecliptic pole, will follow a meridian to the South ecliptic pole and back to the North ecliptic pole by following the antipodal meridian. Such a scan will last one minute and will be repeated sixty times. After that, the rotation axis will be shifted in a precessional motion for 2'5 (approximately half a beam diameter) and the scan repeated. In this way, the entire sky is mapped once in 180 days.

Fourier transform of the noise time series of *Planck*'s receivers yields a noise power spectrum $P(f)$ of the shape

$$P(f) = \sigma_N^2 \cdot \left[1 + \left(\frac{f}{f_{\text{knee}}} \right)^{-\alpha} \right], \quad (6)$$

i.e. the noise consists of two components: a power law component in frequency f , described by the spectral index α that assuming values $0 \leq \alpha \leq 2$ and a white noise component, smoothly joined at the frequency f_{knee} .

The $f^{-\alpha}$ -part of the noise spectrum originates from zero point

¹ <http://planck.mpa-garching.mpg.de/>

² <http://astro.estec.esa.nl/Planck/>

Planck channel	1	2	3	4	5	6	7	8	9
centre frequency ν_0	30 GHz	44 GHz	70 GHz	100 GHz	143 GHz	217 GHz	353 GHz	545 GHz	857 GHz
frequency window $\Delta\nu$	3.0 GHz	4.4 GHz	7.0 GHz	16.7 GHz	23.8 GHz	36.2 GHz	58.8 GHz	90.7 GHz	142.8 GHz
resolution $\Delta\theta$ (FWHM)	33'.4	26'.8	13'.1	9'.2	7'.1	5'.0	5'.0	5'.0	5'.0
noise level σ_N	1.01 mK	0.49 mK	0.29 mK	5.67 mK	4.89 mK	6.05 mK	6.80 mK	3.08 mK	4.49 mK
thermal SZ-flux $\langle S_{\mathcal{Y}} \rangle$	-12.2 Jy	-24.8 Jy	-53.6 Jy	-82.1 Jy	-88.8 Jy	-0.7 Jy	146.0 Jy	76.8 Jy	5.4 Jy
kinetic SZ-flux $\langle S_{\mathcal{W}} \rangle$	6.2 Jy	13.1 Jy	30.6 Jy	55.0 Jy	86.9 Jy	110.0 Jy	69.1 Jy	15.0 Jy	0.5 Jy
antenna temperature $\Delta T_{\mathcal{Y}}$	-440 nK	-417 nK	-356 nK	-267 nK	-141 nK	-0.5 nK	38 nK	8.4 nK	0.2 nK
antenna temperature $\Delta T_{\mathcal{W}}$	226 nK	220 nK	204 nK	179 nK	138 nK	76 nK	18 nK	1.6 nK	0.02 nK

Table 1. Characteristics of *Planck*'s LFI-receivers (column 1-3) and HFI-bolometers (column 4-9): centre frequency ν_0 , frequency window $\Delta\nu$ as defined in eqns. (27) and (28), angular resolution $\Delta\theta$ stated in FWHM, effective noise level σ_N , fluxes $\langle S_{\mathcal{Y}} \rangle$ and $\langle S_{\mathcal{W}} \rangle$ generated by the respective Comptonisation of $\mathcal{Y} = \mathcal{W} = 1$ arcmin² and the corresponding changes in antenna temperature $\Delta T_{\mathcal{Y}}$ and $\Delta T_{\mathcal{W}}$. Due to *Planck*'s symmetric frequency response window, the thermal SZ-effect does not vanish entirely at $\nu = 217$ GHz.

drifts of the detector gain on large time scales. This power law component exhibits low-frequency variations that lead to the typical stripe pattern in simulated *Planck*-maps due to the scanning strategy (Maino et al. 1999). Algorithms for destriping the maps are a current research topic (for example, the *Mirage*-algorithm proposed by Yvon & Mayet (2004), *MAPCUMBA* by Doré et al. (2001) and the max-likelihood algorithm by Natoli et al. (2001)), but it can be expected that the destriping can be done very efficiently such that the remaining noise largely consists of uncorrelated pixel noise.

In order to incorporate uncorrelated pixel noise into the simulation, a set of maps has been constructed, where at each pixel a number from a Gaussian distribution with width σ_N has been drawn. For *Planck*'s HFI-receivers, the rms-fluctuations σ_N in antenna temperature can be calculated from the noise equivalent power NEP and the sampling frequency $\nu_{\text{sampling}} = 200$ Hz via:

$$\sigma_N = \frac{2 \text{ NEP} \sqrt{\nu_{\text{sampling}}}}{k_B \Delta\nu} \quad (\text{HFI}) \quad (7)$$

Alternatively, for *Planck*'s LFI-receivers, the rms-fluctuations σ_N in antenna temperature are given by:

$$\sigma_N = \sqrt{2} \frac{T_{\text{noise}} + T_{\text{CMB}}}{\sqrt{\Delta\nu/\nu_{\text{sampling}}}} \quad (\text{LFI}) \quad (8)$$

Values for T_{noise} and NEP can be obtained from *Planck*'s simulation pipeline manual. The resulting effective noise level for all *Planck* channels for a single observation of a pixel is given in Table 1. The formulae and respective parameters are taken from the *Planck* simulation manual, available via *Planck*'s LiveLink.

The rms-fluctuations σ_N in antenna temperature have to be scaled by $\sqrt{n_{\text{det}}}$ (assuming Poissonian statistics), where n_{det} denotes the number of redundant receivers per channel, because they provide independent surveys of the microwave sky.

From simulated scanning paths it is possible to derive an exposure map using the `simmission`- and `multimod`-utilities. An example of such an exposure map in the vicinity of the North ecliptic pole is given in Fig. 1. Using the number of observations n_{obs} per pixel, it is possible to scale down the noise amplitudes by $\sqrt{n_{\text{obs}}}$ and to obtain a realistic noise map for each channel. Here, we apply the simplification that all detectors of a given channel are arranged collinearly. In this case, the exposure maps will have sharp transitions from well-observed regions around the ecliptic poles to the region around the ecliptic equator. In real observations these transitions will be smoothed out due slight displacements of the optical axes among each other which causes the effective exposure pattern

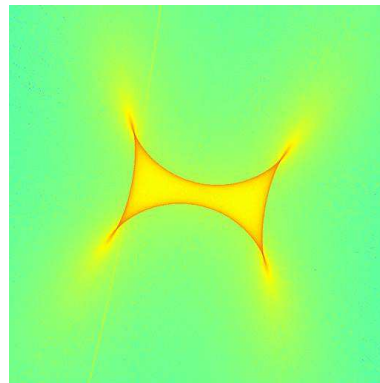


Figure 1. Exposure map (side length $\approx 70^\circ$) of a single $\nu = 353$ GHz-receiver at the North ecliptic pole in logarithmic shading: The displacement of the receiver with respect to the optical axis causes the observational rings not to overlap exactly at the pole, but gives rise to the lozenge-shaped pattern in the sky-coverage map. On average, the pixels inside the lozenge are observed roughly 100 times, compared to ~ 20 times outside. Pixels on the edges of the lozenge are observed a few thousand times. The best observed pixels are situated on the tips of the lozenge, where values as high as $2 \cdot 10^4$ are attained. The numbers correspond to the planned mission lifetime of 1 year. The faint diagonal tangential line on the left side is caused by 2008's being a leap year: The mapping of the entire sky would be completed in 365 days, but there is an additional day available.

to be a superposition of rotated and distorted single-receiver exposure patterns.

4 FOREGROUND EMISSION COMPONENTS

The observation of the CMB and of SZ-clusters is seriously impeded by various Galactic foregrounds and by the thermal emission of celestial bodies of our Solar system. In order to describe these emission components, template maps from microwave surveys are used. Bouchet & Gispert (1999) give a comprehensive review for the foreground components relevant for the *Planck* mission. As foreground components we include thermal emission from dust in the Galactic plane (Sect. 4.1), Galactic synchrotron (Sect. 4.2) and free-free emission (Sect. 4.3), line emission from rotational transitions of carbon monoxide molecules in giant molecular clouds (Sect. 4.4), sub-millimetric emission from planets (Sect. 4.5) and

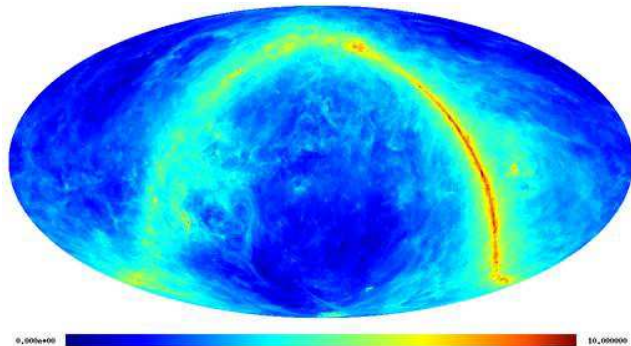


Figure 2. Sky map of the antenna temperature increase caused by dust emission in the $\nu = 100$ GHz-channel: The shading is proportional to $\text{arsinh}(T_A(\nu = 100 \text{ GHz})/\mu\text{K})$. Ecliptic coordinates have been chosen. This map has been derived from the dust-template map provided by Schlegel et al. (1998).

from minor bodies of the Solar system (Sect. 4.6). Foreground components omitted at this stage are discussed in Sect. 4.7.

In this work, no attempt is made at modelling the interactions between various foreground components because of poorly known parameters such as the spatial arrangement along the line-of-sight of the emitting and absorbing components. Exemplarily, the reader is referred to Finkbeiner (2003), where the absorption of Galactic free-free emission by dust is discussed.

4.1 Galactic dust emission

At frequencies above ~ 100 GHz, the thermal emission from dust in the disk of the Milky Way is the most prominent feature in the microwave sky. Considerable effort has been undertaken to model the thermal emission from Galactic dust (Schlegel et al. 1997, 1998; Finkbeiner et al. 1999, 2000). The thermal dust emission is restricted to low Galactic latitudes and the thin disk is easily discernible.

The input template map (see Fig. 2) is derived from an observation at a wavelength of $\lambda = 100 \mu\text{m}$, i.e. $\nu_0 = 3$ THz. Its amplitudes A_{dust} are given in MJy/sr, which are extrapolated to the actual frequency channels of *Planck* using a two-component model suggested by C. Baccigalupi (personal communication). Despite the fact that the dust is expected to spread over a large range of temperatures, the model reproduces the thermal emission remarkably well. This model yields for the flux $S_{\text{dust}}(\nu)$:

$$S_{\text{dust}}(\nu) = \frac{f_1 q \cdot \left(\frac{\nu}{\nu_0}\right)^{\alpha_1} B(\nu, T_1) + f_2 \cdot \left(\frac{\nu}{\nu_0}\right)^{\alpha_2} B(\nu, T_2)}{f_1 q B(\nu_0, T_1) + f_2 B(\nu_0, T_2)} \cdot A_{\text{dust}}. \quad (9)$$

The choice of parameters used is: $f_1 = 0.0363$, $f_2 = 1 - f_1$, $\alpha_1 = 1.67$, $\alpha_2 = 2.70$, $q = 13.0$. The two dust temperatures are $T_1 = 9.4$ K and $T_2 = 16.2$ K. The function $B(\nu, T)$ denotes the Planckian emission-law:

$$B(\nu, T) = \frac{2h}{c^2} \cdot \frac{\nu^3}{\exp(h\nu/k_B T) - 1}. \quad (10)$$

4.2 Galactic synchrotron emission

Relativistic electrons of the interstellar medium produce synchrotron radiation by spiralling around magnetic field lines, which impedes CMB observations most strongly at frequencies below 100 GHz. The synchrotron emission reaches out to high Galactic

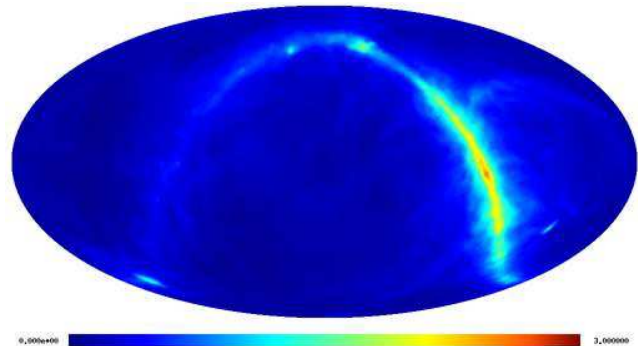


Figure 3. Sky map of the antenna temperature increase caused by synchrotron emission in the $\nu = 100$ GHz-channel in ecliptic coordinates: The shading is proportional to $\text{arsinh}(T_A(\nu = 100 \text{ GHz})/\mu\text{K})$. The survey undertaken by Haslam et al. (1982) was used to construct this template.

latitude and is an important ingredient for modelling foreground emission in microwave observations. An all-sky survey at an observing frequency of 408 MHz has been compiled by Haslam et al. (1981, 1982) and adopted for usage with *Planck* by Giardino et al. (2002) (see Fig. 3). The average angular resolution of this survey is $0'.85$ (FWHM).

Recent observations with WMAP (Bennett et al. 2003) indicate that the spectral slope of the synchrotron emission changes dramatically from $\gamma = -0.75$ at frequencies below 22 GHz to $\gamma = -1.25$ above 22 GHz. Theoretically, this may be explained by a momentum-dependent diffusion coefficient for cosmic ray electrons. In order to take account of this spectral steepening, the amplitudes A_{synchro} are multiplied with a prefactor in order to obtain the synchrotron fluxes at $\nu = 22$ GHz. This value is then extrapolated to *Planck*'s observing frequencies with a spectral index of $\gamma = -1.25$: The amplitudes A_{synchro} of the input map are given in units of MJy/sr, and for the flux $S_{\text{synchro}}(\nu)$ one thus obtains:

$$S_{\text{synchro}}(\nu) = \sqrt{\frac{22 \text{ GHz}}{408 \text{ MHz}}} \cdot A_{\text{synchro}} \cdot \left(\frac{\nu}{408 \text{ MHz}}\right)^{-1.25}. \quad (11)$$

Here, the fact that the synchrotron spectral index shows significant variations across the Milky Way due to varying magnetic field strength is ignored. Instead, a spatially constant spectral behaviour is assumed.

4.3 Galactic free-free emission

The Galactic ionised plasma produces free-free emission, which is an important source of contamination in CMB observations, as recently confirmed by Bennett et al. (2003) in WMAP observations. Aiming at modelling the free-free emission at microwave frequencies, we rely on an H_α -template provided by Finkbeiner (2003). Modeling of the free-free emission component on the basis of an H_α -template is feasible because both emission processes depend on the emission measure $\int n_e^2 dl$, where n_e is the number density of electrons. This template is a composite of three H_α -surveys and is because of its high resolution (on average $6'.0$ FWHM) particularly well suited for CMB foreground modelling. The morphology of the free-free map is very complex and the emission reaches out to intermediate Galactic latitude.

For relating H_α -fluxes A_{H_α} given in units of Rayleighs to the free-free signal's antenna temperature $T_{\text{free-free}}$ measured in Kelvin, Valls-Gabaud (1998) gives the formula:

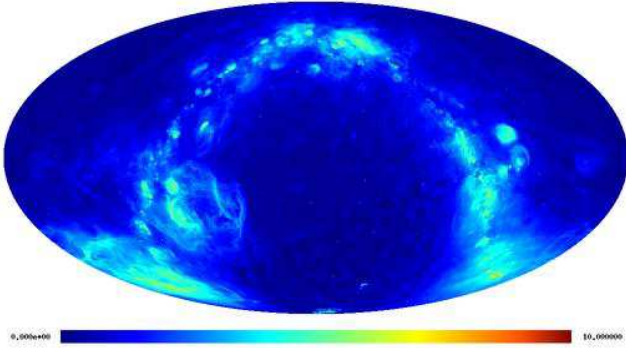


Figure 4. Sky map of the antenna temperature increase caused by free-free emission in the $\nu = 100$ GHz-channel: The shading is proportional to $\text{arsinh}(T_A(\nu = 100 \text{ GHz})/\mu\text{K})$. Ecliptic coordinates have been chosen. This map has been derived from the H_α -template map provided by Finkbeiner (2003).

$$\frac{T_{\text{free-free}}(\mu\text{K})}{A_{H_\alpha}(R)} \simeq 14.0 \left(\frac{T_p}{10^4 \text{ K}} \right)^{0.317} \cdot 10^{290 \text{ K} \cdot T_p^{-1}} \cdot g_{\text{ff}} \cdot \left(\frac{\nu}{10 \text{ GHz}} \right)^{-2}. \quad (12)$$

T_p denotes the plasma temperature and is set to 10^4 K in this work. An approximation for the Gaunt factor g_{ff} valid for microwave frequencies in the range $\nu_p \ll \nu \ll k_B T/h$ (ν_p is the plasma frequency) is given by Finkbeiner (2003):

$$g_{\text{ff}} = \frac{\sqrt{3}}{\pi} \left[\ln \left(\frac{(2k_B T_p)^{3/2}}{\pi e^2 \nu \sqrt{m_e}} \right) - \frac{5}{2} \gamma_E \right], \quad (13)$$

where e and m_e denote electron charge and mass (in Gaussian units) and $\gamma_E \simeq 0.57721$ is the Euler constant. The contribution of fractionally ionised helium to the free-free emissivity as well as the absorption by interstellar dust has been ignored because of its being only a small contribution in the first case and because of poorly known parameters in the latter case. The antenna temperature can be converted to the free-free flux $S_{\text{free-free}}(\nu)$ by means of:

$$S_{\text{free-free}}(\nu) = 2 \frac{\nu^2}{c^2} \cdot k_B T_{\text{free-free}}(\text{K}). \quad (14)$$

Concerning the free-free emission, there might be the possibility of an additional free-free component uncorrelated with the H_α -emission. This hot gas, however, should emit X-ray line radiation, which has not been observed.

4.4 CO-lines from giant molecular clouds

In a spiral galaxy such as the Milky Way, a large fraction of the interstellar medium is composed of molecular hydrogen, that resides in giant molecular clouds (GMC), objects with masses of $10^4 - 10^6 M_\odot$ and sizes of 50 – 200 pc. Apart from molecular hydrogen, the GMCs contain carbon monoxide (CO) molecules in significant abundance. The rotational transitions of the CO molecule at 115 GHz and higher harmonics thereof constitute a source of contamination for all *Planck HFI*-channels. An extensive search for atomic and molecular transition lines was undertaken by Bennett et al. (1994) with the *FIRAS* instrument onboard *COBE*.

The CO-contamination is modelled by employing a mosaic of CO-surveys assembled by Dame et al. (1996, 2001). It shows the velocity-integrated intensity of the transition from the first excited state ($J = 1$) to the ground state ($J = 0$) close to the Galactic plane ($b < 5^\circ$), and additionally comprises a few CO clouds at higher Galactic latitude, as well as the Large Magellanic Cloud and the

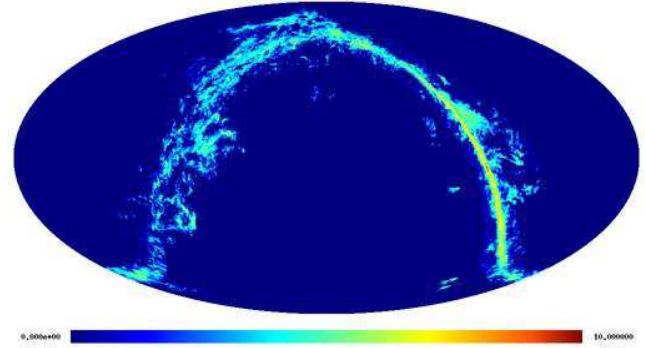


Figure 5. Sky map of the increment in antenna temperature due to CO-line emission in the $\nu = 100$ GHz-channel in ecliptic coordinates: The shading is proportional to $\text{arsinh}(T_A(\nu = 100 \text{ GHz})/\mu\text{K})$. The maps shows the rotational transition of the CO molecule from the first excited state into the ground state at $\nu_{0 \leftrightarrow 1} = 115$ GHz as derived by Dame et al. (2001) for a temperature of $T_{\text{CO}} = 20$ K.

Andromeda galaxy M 31. Due to the composition of the map, the angular resolution is not uniform, but the best resolution of $\simeq 7:5$ is reached for a large area around the Galactic plane.

From this map, it is possible to derive the line intensities of the higher harmonics, assuming thermal equilibrium: The frequency ν for a transition from a state of rotational quantum number J to a state with quantum number $J + 1$ of the CO molecule follows from elementary quantum mechanics: The rotational energy of a molecule with moment of inertia θ and angular momentum \mathbf{J} is $E_{\text{rot}} = \mathbf{J}^2/2\theta = \hbar^2 \cdot J(J+1)/2\theta$. In the last step the quantum number J was introduced. For the transition energy between two subsequent rotation levels, one obtains:

$$\nu_{J \leftrightarrow J+1} = 2Qc \cdot (J + 1) = 115 \text{ GHz} \cdot (J + 1), \quad (15)$$

where $Q = h/8\pi^2 c \theta$ is a measure of the inverse moment of inertia of the molecule and c denotes the speed of light. Thus, the spectrum consists of equidistant lines. The relative intensities of those lines is given by the ratio of their occupation numbers χ_J :

$$\chi_J = (2J + 1) \cdot \exp \left(-\frac{Qhc}{k_B T_{\text{CO}}} J(J + 1) \right), \quad (16)$$

i.e. the relative line intensities $q_{J \leftrightarrow J+1}$ of two consecutive lines is given by:

$$q_{J \leftrightarrow J+1} = \frac{\chi_{J+1}}{\chi_J} = \frac{2J + 3}{2J + 1} \cdot \exp \left(-\frac{2Qhc}{k_B T_{\text{CO}}} \cdot (J + 1) \right) \quad (17)$$

χ_J is determined by a statistical weight $(2J + 1)$ reflecting the degeneracy of angular momentum and a Boltzmann factor. For the determination of line intensities thermal equilibrium is assumed, common estimates for the temperature inside GMCs are $T_{\text{CO}} = 10 - 30$ K. For the purpose of this work, we choose $T_{\text{CO}} = 20$ K. From the brightness temperature T_A one obtains the CO-flux $S_{\text{CO-line}}(\nu)$ by means of the following equation:

$$S_{\text{CO-line}}(\nu) = 2 \frac{\nu^2}{c^2} \cdot k_B T_A(\text{K}) \cdot p(\nu - \nu_{J \leftrightarrow J+1}), \quad (18)$$

where the line shape $p(\nu - \nu_{J \leftrightarrow J+1})$ is assumed to be small in comparison to *Planck's* frequency response windows such that its actual shape (for instance, a Voigt-profile) is irrelevant.

4.5 Planetary submillimetric emission

Planets produce infra-red and sub-millimetric radiation by absorbing sunlight and by re-emitting this thermal load imposed by the sun. The investigation of the thermal properties of Mars, Jupiter and Saturn has been the target of several space missions (Goldin et al. 1997; Griffin et al. 1986, to name but a few). For the description of the submillimetric thermal emission properties of planets, an extension to the Wright & Odenwald model (Wright 1976; Neugebauer et al. 1971) was used. The orbital motion of the planets is sufficiently fast such that their movements including their epicyclic motion relative to the Lagrangian point L_2 , *Planck*'s observing position, has to be taken into account. All planets are imaged twice in approximate half-year intervals due to *Planck*'s scanning strategy, while showing tiny displacements from the ecliptic plane because of the Lissajous-orbit of *Planck* around L_2 and their orbital inclinations.

The heat balance equation for a planet or asteroid reads as:

$$E + F + W \equiv P_{\text{emission}} = P_{\text{absorption}} \equiv I + R, \quad (19)$$

where E denotes the heat loss by thermal emission (i.e. the signal for *Planck*), F the heat flux outward from the interior of the planet, W is the heat lost by conduction to the planet's atmosphere, I is the Solar radiation absorbed and R is the heating of the planet caused by the back-scattering of radiation emanating from the surface of the planet by the atmosphere. The definition of these quantities is given by eqns. (20) through (24):

$$E = \epsilon \sigma T_{\text{planet}}^4, \quad (20)$$

$$F = k \cdot \frac{\partial T_{\text{planet}}}{\partial x}, \quad (21)$$

$$I = \frac{(1-A)G}{r^2} \cos(\theta^*) \cos\left(\frac{2\pi t}{\tau}\right), \quad (22)$$

$$R = \gamma \frac{(1-A)G}{r^2} \cos(\theta^*) \cos\left(\frac{2\pi t}{\tau}\right) = \gamma I_{\text{max}}, \text{ and} \quad (23)$$

$$W = \kappa F. \quad (24)$$

Here, ϵ is the surface emissivity of the planet, σ is the Stefan-Boltzmann constant, T_{planet} is the planet's temperature, k the coefficient of heat conduction, A the planet's bolometric albedo, G the Solar constant (i.e. the energy flux density of Solar irradiation at the earth's mean distance), r the distance of the planet to the sun in astronomical units, τ the planet's rotation period and θ^* the geographical latitude of the radiation absorbing surface element. The temperature distribution in the interior of the planet at radial position x is controlled by the heat conduction equation:

$$c \cdot \frac{\partial T_{\text{planet}}}{\partial t} = k \cdot \frac{\partial^2 T_{\text{planet}}}{\partial x^2}, \quad (25)$$

with the specific heat per unit volume c .

In our model, the heat loss R of the planet's surface due to conduction to the planet's atmosphere is taken to be a constant fraction of the heat flux F outward from the interior of the planet, the constant of proportionality being κ , for which we assumed $\kappa = 0.1$. Similarly, the heat gain by back-scattering radiation by the atmosphere R was assumed to be a constant fraction γ of the local noon Solar flux I_{max} , where γ was taken to be $\gamma = 0.01$. The system of differential eqns. (20) - (24) dependent on time t and on Solar distance r constitutes a heat conduction problem with periodic excitation (by the planet's rotation). Thus, the heat balance of the planets is modelled by periodic solutions of the Laplacian heat conduction

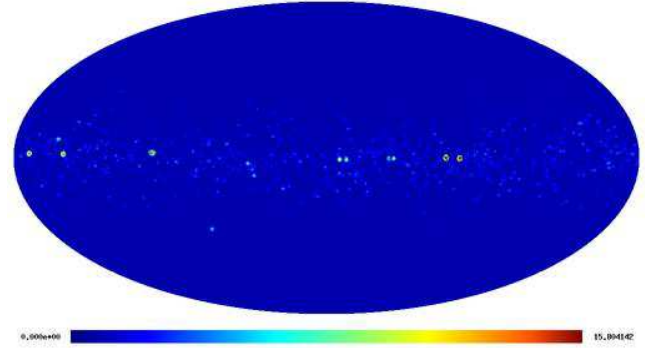


Figure 6. Sky map of increment in antenna temperature T_A produced by planets and asteroids in the $\nu = 30$ GHz channel at $33'4$ resolution (FWHM). The colour coding is proportional to $\text{arsinh}(T_A(\nu = 100 \text{ GHz})/n\text{K})$. The asteroids reach ecliptic latitudes of $|\beta| \lesssim 30^\circ$. The pronounced signals are produced by planets, which (due to *Planck*'s scanning strategy) appear twice. The observable planets comprise (from left to right) Saturn, Mars, Uranus, Neptune and Jupiter. The epicyclic motion of Mars is sufficiently fast to counteract the parallactic displacement such that it appears only once.

differential equations. It was solved iteratively by applying Laplace transforms with periodic boundary conditions. The integration over the planet's surface then yields the radiation flux. In the calculation, we addressed rocky and gaseous planets differently with respect to their thermal properties. Furthermore, the giant gaseous planets are known to have internal sources of heat generation, which also has been taken account of.

The brightest point source in the microwave sky due to the planetary thermal emission is Jupiter, causing an increase in antenna temperature of $T_{\text{Jupiter}} = 93.6$ mK in the $\nu = 100$ GHz-channel, followed by Saturn with $T_{\text{Saturn}} = 15.0$ mK. All outer planets apart from Pluto will be visible for *Planck*. Estimates show that even Galilean satellites Ganymede, Callisto, Io and Europa and Saturn's moon Titan are above the detection threshold of *Planck*, but they are outshone by the stray-light from Jupiter and Saturn, respectively and for that reason not included in our analysis.

Due to the planet's being point sources, their fast movement and their diverse surface temperatures it is not feasible to produce a template and extrapolate the fluxes with a common emission law to *Planck*-frequencies. Instead, flux maps have been produced directly for each of the nine *Planck*-channels separately taking account of the planetary motion, the solution of the heat balance equation laid down above and the finite beam-width. The analogous holds for asteroids, that are covered by the next chapter.

4.6 Submillimetric emission from asteroids

Asteroids and minor bodies of the Solar system are easily observed by infrared satellites such as ISO and possibly by sub-millimetric observatories (Müller 2001; Müller & Lagerros 1999). An estimation by Cremonese et al. (2002) shows that a large number of asteroids (~ 400) should yield signals detectable by *Planck*. The orbital motion of all asteroids is fast enough to cause double detections at different positions in the sky separated by half a year due to *Planck*'s scanning strategy. In contrast to planets, asteroids are not well restricted to the ecliptic plane and appear up to ecliptic latitudes of $\beta \lesssim 30^\circ$.

The thermal emission properties of asteroids are well understood (for a comprehensive and detailed review, see Lagerros

1996a,b, 1997, 1998) such that asteroids have been used for calibrating detectors (e.g. the ISO mission, c.f. Müller & Lagerros 1998, 2002) and for determining beam shapes. The thermal model used for describing the submillimetric emission by asteroids is the same extension of the Wright & Odenwald model as for rocky planets. However, additional features that had to be incorporated was the beamed emission due to surface roughness. Furthermore, in the system of differential eqns. (20) - (24) terms W and R were neglected due to the absence of atmospheres in asteroids.

Information about the diameter and albedo was derived using the HG-magnitude system in case of asteroids for which those quantities are unknown, otherwise literature values were taken (from Moore 2000, and IAU's *Minor Planet Centre*³). For the description of the rotation period, an empirical relation that expresses the rotation period as a function of mass was used in the cases where the rotation period is unknown. The brightest sources include Ceres ($T_{\text{Ceres}} = 19.7 \mu\text{K}$), Pallas ($T_{\text{Pallas}} = 7.2 \mu\text{K}$), Vesta ($T_{\text{Vesta}} = 6.7 \mu\text{K}$) and Davida ($T_{\text{Davida}} = 2.1 \mu\text{K}$). The temperatures stated are antenna temperatures measured in the $\nu = 100 \text{ GHz}$ -channel at the brightness maximum.

Our simulation shows that the number of detectable asteroids is overestimated by Cremonese et al. (2002), who did not take the expected observation geometry and detector response into account. Typical surface temperatures of asteroids are of the order of 150 K, and therefore, *Planck* is observing their thermal emission in the Rayleigh-Jeans regime. For that reason, the number of detectable asteroids increases with observing frequency. For our sample of $5 \cdot 10^4$ asteroids of the *Minor Planet Centre*'s catalogue, we find a couple of asteroids at $\nu = 30 \text{ GHz}$, a few tens of asteroids at $\nu = 100 \text{ GHz}$ and up to 100 asteroids in the highest frequency band at $\nu = 857 \text{ GHz}$. Approximately 1200 asteroids will have fluxes above half of *Planck*'s single-band detection limit estimated for ideal observation conditions and thus they constitute an abundant population of point sources that possibly hampers the detection of SZ-clusters.

The prediction of comets is very uncertain for the years 2007 through 2009: Many comets are not detected yet, non-active comets are too faint with few exceptions and the coma thermal emission features of active comets is very complex. For these reasons, they have been excluded from the analysis.

4.7 Future work concerning *Planck*'s foregrounds

Foreground components not considered so far include microwave point sources, such as infra-red galaxies and microwave emitting AGNs. The emission of infra-red galaxies is associated with absorption of star light by dust and re-emission at longer wavelengths. Galaxies with ongoing star formation can have large fractions ($\sim 90\%$) of their total emission at infra-red wavelengths, compared to about one third in the case of local galaxies. The integrated emission from unresolved infra-red galaxies accounts for the cosmic infra-red background (CIB) (Puget et al. 1996; Lagache & Puget 2000), the fluctuations of which are impeding SZ-observations at frequencies above $\nu \approx 100 \text{ GHz}$ (Aghanim et al. 2004).

Lagache (2003) and White & Majumdar (2003) have estimated the number counts of unresolved infra-red galaxies at *Planck* frequencies, which was used by Aghanim et al. (2004) in order to estimate the level of fluctuation in the *Planck*-beam. In the easiest case, the sources are uncorrelated and the fluctuations obey

Poissonian statistics, but the inclusion of correlations is expected to boost the fluctuations by a factor of ~ 1.7 (Song et al. 2003). According to Aghanim et al. (2004), the resulting fluctuations vary between a few 10^2 Jy/sr and 10^5 Jy/sr , depending on observing channel. A proper modeling would involve a biasing scheme for populating halos, the knowledge of the star formation history and template spectra in order to determine the K-corrections.

AGNs are another extragalactic source of submillimetric emission. Here, synchrotron emission is the radiation generating mechanism. The spectra show a variety of functional behaviours, with spectral indices α generally ranging from -1 to -0.5, but sources with inverted spectra $\alpha > 0$ are commonplace. This variety makes it difficult to extrapolate fluxes to observing frequencies of CMB experiments. Two studies (Toffolatti et al. 1998; Sokasian et al. 2001) have estimated the fluctuations generated by radio emitting AGNs at SZ-frequencies and found them to amount to $10^3 - 10^4 \text{ Jy/sr}$. However, AGNs are known to reside in high-density environments and the proper modelling would involve a (poorly known) biasing scheme in order to assign AGN to the dark matter halos. Apart from that, one would have to assume spectral properties from a wide range of spectral indices and AGN activity duty cycles. Therefore, the study of extragalactic sources has been omitted from this analysis.

Yet another source of microwave emission in the Solar system is the zodiacal light (Leinert et al. 2002; Reach et al. 2003a). Modelling of this emission component is very difficult due to the Lissajous-orbit of *Planck* around the Lagrangian point L_2 . The disk of interplanetary dust is viewed under varying angles depending on the orbital period and the integration over the spatially non-uniform emission features is very complicated. Reach et al. (2003b) have investigated the thermal emission by interplanetary dust from measurements by ISO and have found dust temperatures of $T_{\text{zodiacal}} = 250 - 300 \text{ K}$ and fluxes on the level of $\approx 10^3 \text{ Jy/sr}$, i.e. the equilibrium temperature is separated by two orders of magnitude from the CMB temperature, which means that the intensities are suppressed by a factor of $\sim 10^4$ due to the Rayleigh-Jeans regime of the zodiacal emission in which *Planck* is observing and by a factor of 10^5 due to *Planck*'s narrow beams. From this it is concluded that the emission from zodiacal light is unlikely to exceed values of a few $\sim \mu\text{Jy}$ in observations by *Planck* which compares to the fluxes generated by faint asteroids. Thus, the zodiacal light constitutes only a weak foreground emission component at submillimetric wavelengths and can safely be neglected.

5 SIMULATING SZ-OBSERVATIONS BY *Planck*

The simulation for assessing *Planck*'s SZ-capabilities proceeds in four steps. Firstly, all-sky maps of the thermal and kinetic SZ-effects are prepared, the details of map-construction are given in Sect. 5.1. Secondly, a realisation of the CMB was prepared for the assumed cosmological model (Sect. 5.2). The amplitudes were co-added with the Galactic and ecliptic foregrounds introduced in the previous section, subsequently degraded in resolution with *Planck*'s beams (Sect. 5.3). Finally, uncorrelated pixel noise as well as the emission maps comprising planets and asteroids were added. In the last section, cross-correlation properties of the various astrophysical and instrumental noise components are discussed (Sect. 5.4).

At this stage it should be emphasised that we work exclusively with spherical harmonics expansion coefficients $a_{\ell m}$ of the

³ <http://cfa-www.harvard.edu/cfa/ps/mpc.html>

flux maps. The expansion of a function $a(\theta)$ into spherical harmonics $Y_\ell^m(\theta)$ and the corresponding inversion is given by:

$$a_{\ell m} = \int d\Omega a(\theta) \cdot Y_\ell^m(\theta)^* \text{ and } a(\theta) = \sum_{\ell=0}^{\infty} \sum_{m=-\ell}^{+\ell} a_{\ell m} \cdot Y_\ell^m(\theta). \quad (26)$$

Here, $d\Omega$ denotes the differential solid angle element. For reasons of computational feasibility, we assume isotropic spectral properties of each emission component, i.e. the template map is only providing the amplitude of the respective emission component, but the spectral dependences are assumed to remain the same throughout the sky. While this is an excellent approximation for the CMB and the SZ-effects (in the non-relativistic limit), it is a serious limitation for Galactic foregrounds, where e.g. the synchrotron spectral index or the dust temperatures show significant spatial variations.

Adopting this approximation, the steps in constructing spherical harmonics expansion coefficients $\langle S_{\ell m} \rangle_{\nu_0}$ of the flux maps $S(\theta, \nu)$ for all *Planck* channels consist of deriving the expansion coefficients of the template, converting the template amplitudes to flux units, extrapolate the fluxes with a known or assumed spectral emission law to *Planck*'s observing frequencies, to finally convolve the emission law with *Planck*'s frequency response window for computing the spherical harmonics expansion coefficients of the average measured flux $\langle S_{\ell m} \rangle_{\nu_0}$ at nominal frequency ν_0 by using eqn. (27).

$$\langle S_{\ell m} \rangle_{\nu_0} = \frac{\int d\nu S_{\ell m}(\nu) R_{\nu_0}(\nu)}{\int d\nu R_{\nu_0}(\nu)} = 2 \frac{\nu_0^2}{c^2} \cdot k_B T_{\ell m}. \quad (27)$$

Here, $S_{\ell m}(\nu)$ describes the spectral dependence of the emission component considered, and $R_{\nu_0}(\nu)$ the frequency response of *Planck*'s receivers centered on the fiducial frequency ν_0 . Assuming spatial homogeneity of the spectral behaviour of each emission component it is possible to decompose $S_{\ell m}(\nu)$ into $S_{\ell m}(\nu) = q(\nu) \cdot a_{\ell m}$, i.e. a frequency dependent function $q(\nu)$ and the spherical harmonics expansion coefficients $a_{\ell m}$ of the template describing the morphology. This is possible due to the fact that the decomposition eqn. (26) is linear. Additionally, eqn. (27) gives the conversion from the averaged flux $\langle S_{\ell m} \rangle_{\nu}$ in a *Planck*-channel to antenna temperature $T_{\ell m}$.

Planck's frequency response function $R_{\nu_0}(\nu)$ is well approximated by a top-hat function:

$$R_{\nu_0}(\nu) = \begin{cases} 1, & \nu \in [\nu_0 - \Delta\nu, \nu_0 + \Delta\nu] \\ 0, & \nu \notin [\nu_0 - \Delta\nu, \nu_0 + \Delta\nu] \end{cases} \quad (28)$$

The centre frequencies ν_0 and frequency windows $\Delta\nu$ for *Planck*'s receivers are summarised in Table. 1. In this way it is possible to derive a channel-dependent prefactor relating the flux expansion coefficients $\langle S_{\ell m} \rangle_{\nu_0}$ to the template expansion coefficients $A_{\ell m}$. The superposition of the various emission components in spherical harmonics and the determination of response-folded fluxes is most conveniently done using the `almixer`-utility of *Planck*'s simulation package.

5.1 SZ-map preparation

For constructing an all-sky Sunyaev-Zel'dovich map, a hybrid approach has been pursued. Due to the SZ-clusters being detectable out to very large redshifts, due to their clustering properties on very large angular scales, and due to the requirement of reducing cosmic variance when simulating all-sky observations as will be performed by *Planck*, there is the need for very large simulation boxes, encompassing redshifts of $z \approx 1$ which corresponds to comoving

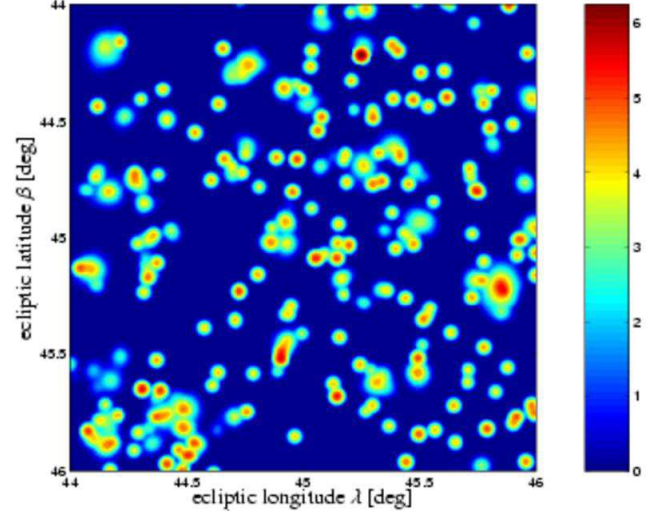


Figure 7. Detail of the thermal Comptonisation map: A $2^\circ \times 2^\circ$ wide cut-out centered on the ecliptic coordinates $(\lambda, \beta) = (45^\circ, 45^\circ)$ is shown. The smoothing imposed was a Gaussian kernel with $\Delta\theta = 2'.0$ (FWHM). The shading indicates the value of the thermal Comptonisation y , which is proportional to $\text{arsinh}(10^6 \cdot y)$. This map resulted from a projection on a Cartesian grid with mesh size $\sim 14''$, i.e. no HEALPix pixelisation can be seen.

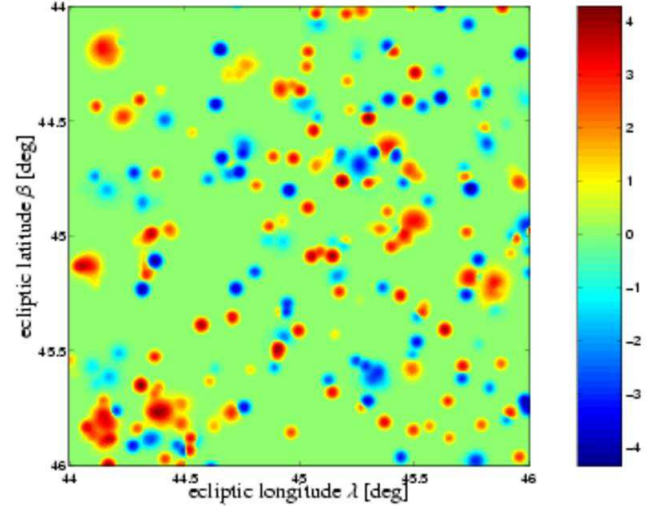


Figure 8. Detail of the kinetic Comptonisation map: A $2^\circ \times 2^\circ$ wide cut-out centered on the same position as Fig. 7, i.e. at the ecliptic coordinates $(\lambda, \beta) = (45^\circ, 45^\circ)$ is shown. The smoothing imposed was a Gaussian kernel with $\Delta\theta = 2'.0$ (FWHM). The kinetic Comptonisation w is indicated by the shading, being proportional to $\text{arsinh}(10^6 \cdot w)$.

scales exceeding 2 Gpc. Unfortunately, a simulation incorporating dark matter and gas dynamics that covers cosmological scales of that size down to cluster scales and possibly resolving cluster substructure is beyond computational feasibility. For that reason, two simulations have been combined: The Hubble-volume simulation (Jenkins et al. 2001; Colberg et al. 2000), and a smaller scale simulation including (adiabatic) gas physics by White et al. (2002) performed with `GADGET` (Springel et al. 2001; Springel & Hernquist 2002).

All-sky maps of the SZ-sky were constructed by using the light-cone output of the Hubble-volume simulation as a cluster catalogue and template clusters from the small-scale gas-dynamical

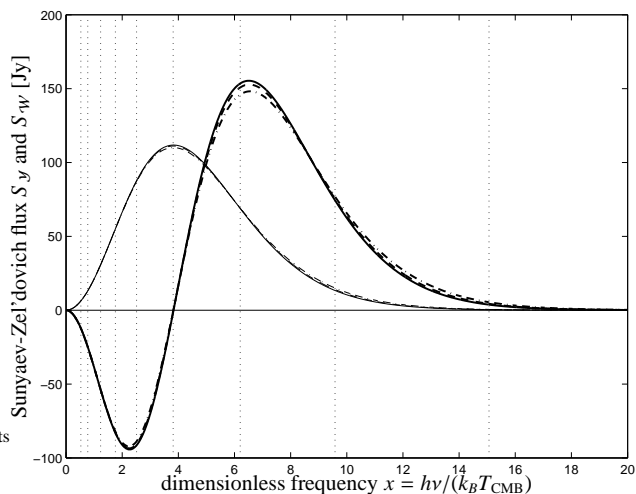


Figure 9. Frequency dependence of the thermal (thick lines) and of the kinetic SZ-flux (thin lines), for ideal δ -like frequency responses (solid lines), for a top-hat window function with a relative width of 10% corresponding to *Planck*'s *LFI*-instrument and for a top-hat window function with a relative width of 16.7%, as planned for *Planck*'s *HFI*-instrument. The fluxes stated correspond to the integrated Comptonisation of $\mathcal{Y} = \mathcal{W} = 1 \text{ arcmin}^2$. The vertical lines indicate the centre frequencies of *Planck*'s receivers.

simulation. In this way, the sky-maps contain all clusters above $5 \cdot 10^{13} M_{\odot}/h$ out to redshift $z = 1.48$. The analysis undertaken by Bartelmann (2001) gives expected mass and redshift ranges for detectable thermal SZ-clusters, which are covered completely by the all-sky SZ-map presented here. The maps show the correct 2-point halo correlation function, incorporate the evolution of the mass function and the correct distribution of angular sizes.

Furthermore, they exhibit cluster substructure and deviations from the ideal cluster scaling relations induced by the departure from spherical symmetry. The velocities used for computing the kinetic SZ-effect correspond to the ambient density field. The map construction process and the properties of the resulting map are in detail described in Schäfer et al. (2004). Visual impressions of the SZ-maps are given by Figs. 7 and 8.

The fluxes generated by the thermal SZ-effect $S_{\mathcal{Y}}(x)$ and of the kinetic SZ-effect $S_{\mathcal{W}}(x)$ are given by eqns. (29) and (30), respectively. The dimensionless frequency is defined as $x = hv/(k_B T_{\text{CMB}})$ and the flux density of the CMB is given by $S_0 = (k_B T_{\text{CMB}})^3 \pi^3 / c^2 / h^2 / 5400 = 22.9 \text{ Jy/arcmin}^2$:

$$S_{\mathcal{Y}}(x) = S_0 \cdot \mathcal{Y} \cdot \frac{x^4 \cdot \exp(x)}{(\exp(x) - 1)^2} \cdot \left[x \frac{\exp(x) + 1}{\exp(x) - 1} - 4 \right]. \quad (29)$$

$$S_{\mathcal{W}}(x) = S_0 \cdot \mathcal{W} \cdot \frac{x^4 \cdot \exp(x)}{(\exp(x) - 1)^2}. \quad (30)$$

Table 1 summarises the fluxes $S_{\mathcal{Y}}$ and $S_{\mathcal{W}}$ and the corresponding changes in antenna temperature $T_{\mathcal{Y}}$ and $T_{\mathcal{W}}$ for the respective Comptonisation of $\mathcal{Y} = \mathcal{W} = 1 \text{ arcmin}^2$ for all *Planck*-channels.

Fig. 9 shows how the frequency dependence of the SZ-signal is altered by *Planck*'s relatively broad frequency response functions. The relative deviations of curves in which the frequency window has been taken into account to the unaltered curve amounts to 5...15%, depending on observation frequency.

5.2 CMB-map generation

The angular power spectrum C_{ℓ} is computed for a flat Λ CDM-cosmology using the *CMBfast* code by Seljak & Zaldarriaga (1996). In addition to the cosmological parameters being already given in Sect. 1, we use adiabatic initial conditions, set the CMB monopole to $T_{\text{CMB}} = 2.725 \text{ K}$ (Mather et al. 1999) and the primordial He-mass fraction to $X_{\text{He}} = 0.24$. The reionisation optical depth τ was set to $\tau = 0.17$ and the reionisation redshift was taken to be $z_{\text{reion}} = 20$ (Bennett et al. 2003). The angular power spectrum of the CMB is normalised to COBE data. With the spectrum of C_{ℓ} -coefficients, a set of $a_{\ell m}$ -coefficients was synthesised by using the *synalm* code based on *synfast* by Hivon et al. (1998). The factors for converting the $a_{\ell m}$ -coefficients of the CMB map showing the thermodynamic temperature and to the corresponding fluxes for each channel were then derived by convolution of the Planckian emission law eqn. (31),

$$S_{\text{CMB}}(\nu) = S_0 \cdot \frac{x^3}{\exp(x) - 1}, \quad (31)$$

with *Planck*'s frequency response function eqns. (27) and (28). Again, $S_0 = 22.9 \text{ Jy/arcmin}^2$ is the energy flux density of the CMB.

5.3 Preparation of simulation data sets

The expansion coefficients of the flux maps are multiplied with the respective beam's $b_{\ell 0}$ -coefficients in order to describe the finite angular resolution. After that, expansion coefficients of the pixel noise maps and those of the planetary maps have been added. In total, three atlases consisting of nine flux $\langle S_{\ell m} \rangle_{\nu_0}$ -sets belonging to each of *Planck*'s channels with fiducial frequency ν_0 have been compiled:

- The reference data set is a combination of the CMB, the SZ-maps and the instrumental noise maps. They should provide the cleanest detection of clusters and the measurement of their properties. Apart from the inevitable instrumental noise, this data set only contains cosmological components. In the remainder of the paper, this data set will be referred to as COS.
- The second data set adds Galactic foregrounds to the CMB, the SZ-maps and the instrumental noise map. Here, we try to assess the extend to which Galactic foregrounds impede the SZ-observations. Thus, this data set will be denoted GAL.
- In the third data set the emission from bodies inside the Solar system was included to the CMB, the SZ-maps, the Galactic foregrounds and the instrumental noise. Because of the planets and asteroids being loosely constrained to the ecliptic plane, this data set will be called ECL.

An example of a synthesised map showing the combined emission of the SZ-clusters and all Galactic and ecliptic components including neither CMB fluctuations nor instrumental noise at a location close to the Galactic plane is given by Fig. 10. The observing frequency has been chosen to be $\nu = 143 \text{ GHz}$, correspondingly, the map has been smoothed with a (Gaussian) beam of $\Delta\theta = 7'.1$ (FWHM).

5.4 Planck-channel correlation properties

In this section the auto- as well as the cross-correlation properties of the various foregrounds in different *Planck*-channels are studied. The cross power spectra, defined formally by eqn. (37) are determined by using:

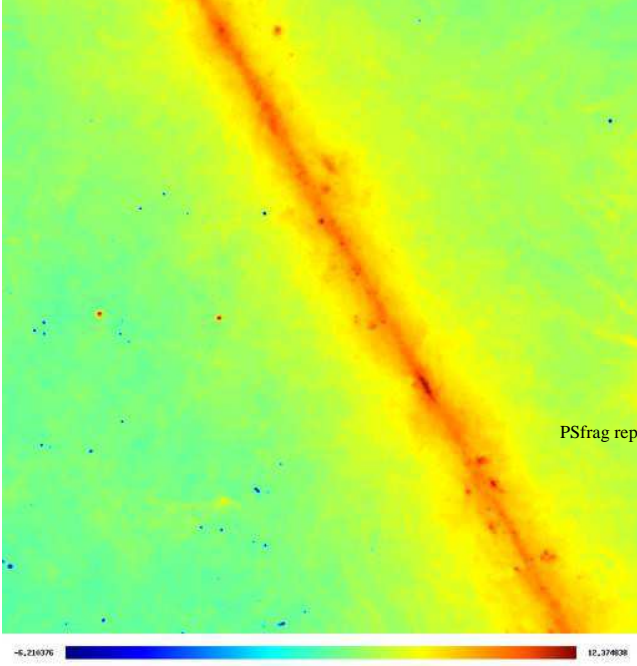


Figure 10. A $50^\circ \times 50^\circ$ wide composite centered on the ecliptic coordinates $(\lambda, \beta) = (-85^\circ, 0^\circ)$, i.e. close to the Galactic centre for *Planck*'s $\nu = 143$ GHz-channel. The shading is proportional to $\text{arsinh}(T_A(\nu = 143 \text{ GHz})/\mu\text{K})$. The map is smoothed with the corresponding beam of diameter $\Delta\theta = 7.1$ (FWHM). SZ-clusters are observed in absorption in this channel and are discernible by eye even at close proximity ($b \lesssim 20^\circ$) to the Galactic plane. For clarity, the CMB fluctuations as well as the instrumental noise have been excluded. The two point sources on the ecliptic equator are twin detections of Jupiter.

$$C_{\ell, \nu_1 \nu_2} = \frac{1}{2\ell + 1} \sum_{m=-\ell}^{+\ell} \langle S_{\ell m} \rangle_{\nu_1} \cdot \langle S_{\ell m} \rangle_{\nu_2}^* \quad (32)$$

From this definition, the auto-correlation spectra are obtained by setting $\nu_1 = \nu_2$, i.e. $C_{\ell, \nu} = C_{\ell, \nu\nu}$. The band-pass averaged fluxes $\langle S_{\ell m} \rangle_\nu$ are defined in eqn. (27). In Fig. 11, the power spectra are shown for the $\nu = 30$ GHz-, $\nu = 143$ GHz-, $\nu = 353$ GHz- and the $\nu = 847$ GHz-channels. The spectra have been derived including various Galactic and ecliptic noise components in order to study their relative influences. For visualisation purposes, the spectra are smoothed with a moving average filter with a filter window comprising 11 bins.

Distinct acoustic peaks of the CMB are clearly visible in the clean COS data sets, but are overwhelmed by the Galactic noise components. At small scales, i.e. high multipole order ℓ , differences between the GAL and ECL data sets become apparent, the latter showing a higher amplitude. The (single) acoustic peak measurable in the $\nu = 33$ GHz channel is shifted to larger angular scales due to the coarse angular resolution of that particular channel. The $\nu = 857$ GHz-curve of the COS data set behaves like a power law due to the fact that the CMB is observed in the Wien-regime and is consequently strongly suppressed, such that the angular power spectrum is dominated by uncorrelated pixel noise.

Fig. 12 shows exemplarily a couple of cross power spectra. The cross-correlation spectra derived for the COS data set nicely shows the CMB power spectrum if two neighboring channels close to the CMB maximum are chosen, but the correlation is lost in two widely separated channels. This is especially the case if one con-

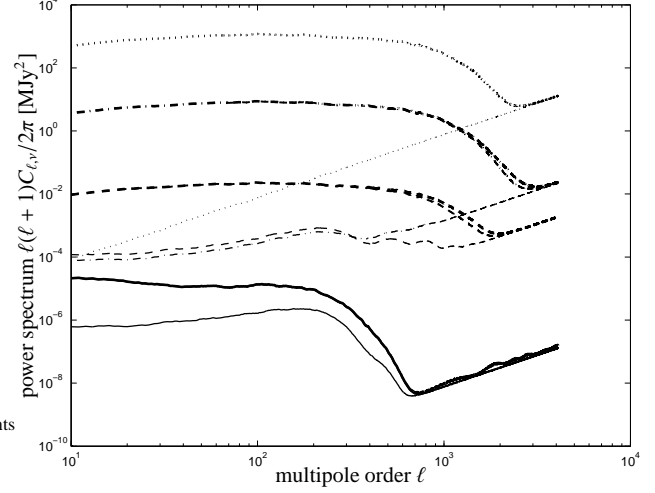


Figure 11. Power spectra in various *Planck*-channels: $\nu = 30$ GHz (solid), $\nu = 143$ GHz (dashed), $\nu = 353$ GHz (dash-dotted) and $\nu = 857$ GHz (dotted) for COS data set (thin line), the GAL data set (medium line) and the ECL data set (thick line).

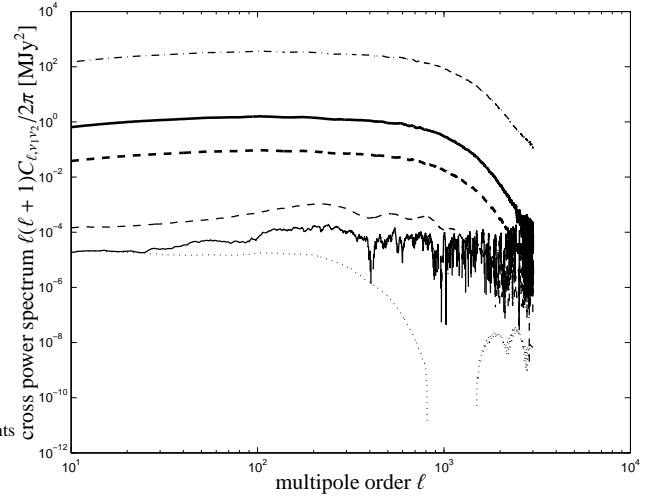


Figure 12. Cross-correlations: The spectra $C_{\ell, \nu_1=143 \text{ GHz}, \nu_2=545 \text{ GHz}}$ (solid line) and $C_{\ell, \nu_1=143 \text{ GHz}, \nu_2=217 \text{ GHz}}$ (dashed line) are contrasted for the COS data set (thin lines) versus the GAL data set (thick line). Furthermore, the spectrum $C_{\ell, \nu_1=545 \text{ GHz}, \nu_2=857 \text{ GHz}}$ (dash-dotted line) as well as $C_{\ell, \nu_1=30 \text{ GHz}, \nu_2=44 \text{ GHz}}$ (dotted line) is shown as derived from the ECL data set.

siders the two lowest *LFI*-channels at angular scales which the receivers are not able to resolve. In this regime the pixel noise is still very small and the cross-correlation spectrum drops to very small values.

In order to illustrate the complexity of spectral and morphological behaviour of the power spectra, they are given as contour plots depending on both the observing frequency ν and the multipole order ℓ . Fig. 13 and 14 contrast the auto-correlation properties of the different data sets. The COS data set, shown in Fig. 13, containing nothing but the CMB and instrumental noise apart from the SZ-contribution, shows clearly the acoustic oscillations with the first peak at $\ell \approx 200$ and the consecutive higher harmonics. They are most pronounced in the $\nu = 100$ GHz- and $\nu = 143$ GHz-channels. At higher multipole moments, the power spectra are dom-

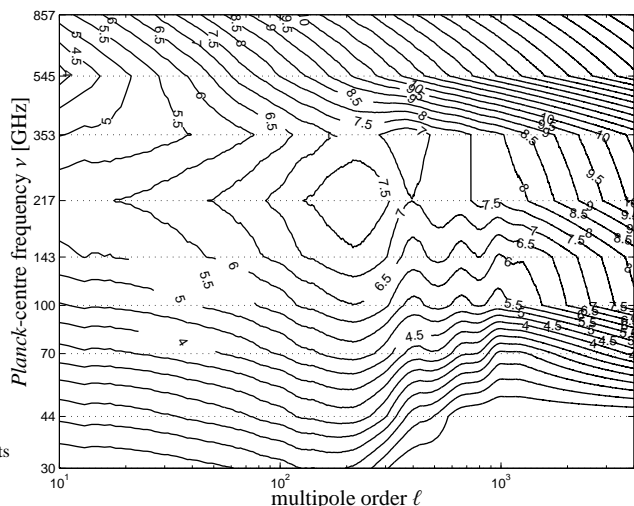


Figure 13. Auto-correlations: The power spectral $C_{\ell,\nu}$ -coefficients are shown as a function of observing frequency ν and multipole order ℓ in the usual representation $\ell(\ell + 1)C_{\ell,\nu}/2\pi$. The amplitudes are given in μK^2 and the contours are linearly spaced. Note the logarithmic scaling of the frequency axis. In the data set displayed, the CMB, both SZ-effects and instrumental noise are included. The first three acoustic oscillation peaks are clearly visible.

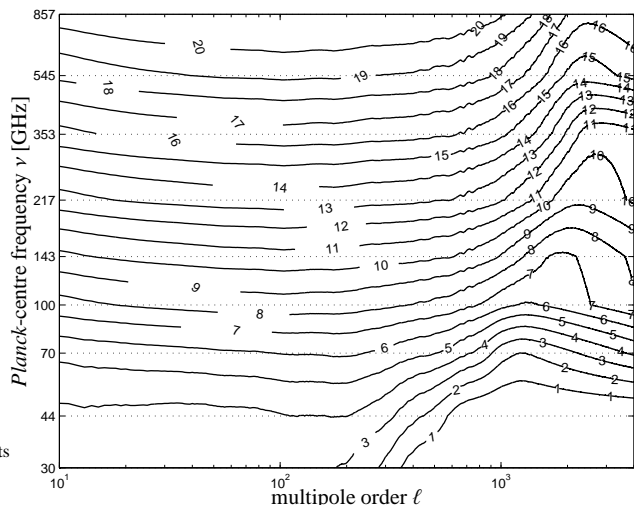


Figure 14. Auto-correlations: The power spectral $C_{\ell,\nu}$ -coefficients are shown as a function of observing frequency ν and multipole order ℓ in the usual representation $\ell(\ell + 1)C_{\ell,\nu}/2\pi$. The amplitudes are given in $\log(\mu\text{K}^2)$ with logarithmically equidistant contours. In the data set displayed, the CMB, both SZ-effects, all Galactic foregrounds and instrumental noise are included.

inated by instrumental noise which leads to a rapid (power law) incline.

Adding Galactic foregrounds yields the spectra depicted in Fig. 14. Inclusion of Galactic foregrounds significantly complicates the picture and masks off the primary anisotropies. The spectra are dominated by large-scale emission structures of the Milky Way, most notably the emission from thermal dust that causes the spectra to increase with increasing frequency ν .

6 CLUSTER DETECTION BY USING MULTI-FREQUENCY OPTIMISED FILTERING

One challenge in the analysis of two-dimensional all-sky surveys is the extraction of sources of interest which are superposed on a background of noise of varying morphology and spectral behaviour. In the presence of small-scale noise the conventional method to extract sources is low-pass filtering (e.g. with a Gaussian kernel) while wavelet analysis is most suitably applied if large scale noise fluctuations dominate. These methods, however, fail if the characteristic scale of the background fluctuations is comparable with the scale of the signal structures. Other methods have been proposed in order to separate different components in multifrequency CMB observations: They include Wiener filtering (Tegmark & Efstathiou 1996; Bouchet & Gispert 1999; Bouchet et al. 1999), maximum-entropy methods (Hobson et al. 1998, 1999), Mexican-hat wavelet analysis (Vielva et al. 2001; Cayón et al. 2000), fast independent component analysis (Maino et al. 2002), matched filter analysis (Tegmark & de Oliveira-Costa 1998), adaptive filtering techniques (Sanz et al. 2001; Herranz et al. 2002b,a), and non-parametric Bayesian approaches (Diego et al. 2002).

However, a comparison between these methods is difficult because all of them assume different priors about the spatial properties and frequency dependence. Using prior knowledge about the frequency dependence and statistical properties of several images at different frequency channels, the maximum-entropy method and Wiener filtering are able to separate the components of interest. Contrarily, wavelet analysis is well suited in order to detect compact sources. A combination of these different techniques improves the quality of component separation (Vielva et al. 2001). Although component separation methods which assume a prior knowledge about the data are quite powerful, they yield biased or even wrong results in the case of incorrect or idealised assumptions about the data. Any error in the separation of one component propagates to the separation of the other components owing to normalisation constraints. In particular, this is the case in non-centrally symmetric source profiles, oversimplified spectral extrapolations of Galactic emission surveys into other wavebands, variations of the assumed frequency dependence, or non-Gaussian noise properties the statistics of which can not fully be characterised by power spectra. Thus, the application of a specific component separation method is a trade-off between robustness and effectiveness with regard to the particular problem.

Filtering techniques relying on Mexican-hat wavelets and on matched and scale-adaptive filters are single component separation methods. They all project either spatial structure or frequency properties (within a given functional family) of the component of interest in the presence of other components acting as background in this context. While Mexican-hat wavelet analysis assumes Gaussian profiles superimposed on large scale variations of the background noise, the matched and scale-adaptive filter generalises to arbitrary source profiles and noise properties which are assumed to be locally homogeneous and isotropic (Sanz et al. 2001; Herranz et al. 2002a,b).

This section generalises the matched and scale-adaptive filter techniques to global spherical topologies which find application in all-sky surveys such as the case of *Planck*'s microwave/submillimetric survey. In addition, optimised filters for the detection of compact sources in single frequency all-sky observations are derived in the appendix in a more detailed fashion. The proposed method aims at simultaneously localising SZ-clusters and measuring both their amplitudes and angular extent. It can also be

applied for localising microwave point sources and estimating their spectral properties.

We choose the spherical filtering approach rather than tiling the sky with a set of two-dimensional flat maps for the following reasons: On the sphere, we do not have to worry about spurious detections as well as double detections due to overlaps in the tessellation. Secondly, our approach provides a physical interpretation of our filter shapes in harmonic space even for the smallest multipole moments in contrast to the case of a flat map where the smallest wavenumbers are determined by the map size. Finally, our approach circumvents projection failures of the noise properties such as stretching effects in the case of conformal mapping which would introduce artificial non-Gaussianity in our maps and distort profile shapes close to the map boundaries.

We pursue the concept of the *multi-frequency approach* rather than the *combination method* (c.f. Herranz et al. 2002a). In other words, we filter each channel separately while taking into account the different cross-correlations between the different channels and the frequency dependence of the signal when constructing the optimised filters. This method seems to be superior to the *combination method* which tries to find a optimised combination of the different channels with regard to the signal-to-noise ratio of the sources and successively applies filters to the combined map.

The concept is introduced and central definitions are laid down in Sect. 6.1. The concept of constructing filter kernels is outlined in Sect. 6.2. Subsequently, the matched and scale-adaptive filters are derived for expansions of spherical data sets into spherical harmonics in Sect. 6.3 and Sect. 6.4. Then, the numbers of merit are defined in Sect. 6.5. Caveats in the numerical derivation are listed in Sect. 6.6. A discussion of filter kernel shapes in Sect. 6.7 for actual simulation data. The application of the filter kernels to our simulated sky maps and the extraction of the SZ-cluster signal is described in Sect. 6.8.

6.1 Assumptions and definitions

When constructing the particular filters, we assume centrally symmetric profiles of the sources to be detected. This approximation is justified for most of the clusters of *Planck*'s sample whose angular extent will be comparable in size to *Planck*'s beams, i.e. the instrumental beam renders them azimuthally symmetric irrespective of their intrinsic shape. Azimuthal symmetry is no general requirement for the filters which can be generalised to detect e.g. elliptical clusters using expansions into vector rather than scalar spherical harmonics.

We furthermore assume the background to be statistically homogeneous and isotropic, i.e. a complete characterisation can be given in terms of the power spectrum. This assumption obviously fails for non-Gaussian emission features of the Galaxy or of the exposure-weighted instrumental noise on large angular scales. However, the spherical harmonics expansion of any expected compact source profile, which we aim to separate, peaks at high values of the multipole moment due to the smallness of the clusters where the non-Gaussian influence is negligible. Thus, we only have to require homogeneity and isotropy of the background on small scales.

In order to construct our filters, we consider a set of all-sky maps of the detected scalar field $s_\nu(\boldsymbol{\theta})$ for the different frequency channels

$$s_\nu(\boldsymbol{\theta}) = f_\nu y_\nu(|\boldsymbol{\theta} - \boldsymbol{\theta}_0|) + n_\nu(\boldsymbol{\theta}), \quad \nu = 1, \dots, N, \quad (33)$$

where $\boldsymbol{\theta} = (\theta, \varphi)$ denotes a two-dimensional vector on the sphere,

$\boldsymbol{\theta}_0$ is the source location, and N is the number of frequencies (respectively, the number of maps). The first term on the right-hand side represents the amplitude of the signal caused by the thermal and kinetic SZ-effect, $y(|\boldsymbol{\theta} - \boldsymbol{\theta}_0|)$ and $w(|\boldsymbol{\theta} - \boldsymbol{\theta}_0|)$, respectively, while the second term corresponds to the generalised noise which is composed of CMB radiation, all Galactic and ecliptic emission components, and additional instrumental noise. The frequency dependence of the SZ-effect is described by f_ν in terms of average flux,

$$f_\nu \equiv \langle S_{\mathcal{Y}} \rangle_\nu, \text{ and } f_\nu \equiv \langle S_{\mathcal{W}} \rangle_\nu, \quad (34)$$

where $\langle S \rangle_\nu$ denotes the flux weighted by the frequency response at the fiducial frequency ν (c.f. eqn. (27)) and $S_{\mathcal{Y}}$ and $S_{\mathcal{W}}$ denote the SZ-fluxes given by eqns. (29) and (30).

We expect a multitude of clusters to be present in our all-sky maps. In order to sketch the construction of the optimised filter, we assume an individual cluster situated at the North pole ($\boldsymbol{\theta}_0 = \mathbf{0}$) with a characteristic angular SZ-signal $y_\nu(\theta = |\boldsymbol{\theta}|) = A\tau_\nu(\theta)$, where we separate the true amplitude A and the spatial profile normalised to unity, $\tau_\nu(\theta)$. The underlying cluster profile $p(\theta)$ is assumed to follow a generalised King-profile with an exponent λ which is a parameter in our analysis. At each observation frequency this profile is convolved with the (Gaussian) beam of the respective *Planck*-channel (c.f. Sect. 3.1) yielding:

$$\tau_\nu(\theta) = \int d\Omega' p(\theta') b_\nu(|\boldsymbol{\theta} - \boldsymbol{\theta}'|) = \sum_{\ell=0}^{\infty} \tau_{\ell 0, \nu} Y_\ell^0(\cos \theta), \quad (35)$$

$$p(\theta) = \left[1 + \left(\frac{\theta}{\theta_c} \right)^2 \right]^{-\lambda}, \quad \text{and} \quad \tau_{\ell 0, \nu} = \sqrt{\frac{4\pi}{2\ell + 1}} b_{\ell 0, \nu} p_{\ell 0}. \quad (36)$$

For the second step in eqn. (36) we used the convolution theorem on the sphere to be derived in Appendix A. The background $n_\nu(\boldsymbol{\theta})$ is assumed to be a compensated homogeneous and isotropic random field with a cross power spectrum $C_{\ell, \nu_1 \nu_2}$ defined by

$$\langle n_{\ell m, \nu_1} n_{\ell' m', \nu_2}^* \rangle = C_{\ell, \nu_1 \nu_2} \delta_{\ell \ell'} \delta_{m m'}, \quad \text{where} \quad \langle n_\nu(\boldsymbol{\theta}) \rangle = 0, \quad (37)$$

$n_{\ell m, \nu}$ denotes the spherical harmonics expansion coefficient of $n_\nu(\boldsymbol{\theta})$, $\delta_{\ell \ell'}$ denotes the Kronecker symbol, and $\langle \cdot \rangle$ corresponds to an ensemble average. Assuming ergodicity of the field under consideration allows taking spatial averages over sufficiently large areas $\Omega = O(4\pi)$ instead of performing the ensemble average.

6.2 Concepts in filter construction

The idea of an optimised matched filter for multifrequency observations was recently proposed by Herranz et al. (2002a) for the case of a flat geometry. For each observing frequency, we aim at constructing a centrally symmetric optimised filter function $\psi_\nu(\boldsymbol{\theta})$ operating on a sphere. Its functional behaviour induces a family of filters $\psi_\nu(\boldsymbol{\theta}, R_\nu)$ which differ only by a scaling parameter R_ν . For a particular choice of this parameter, we define the filtered field $u_\nu(R_\nu, \boldsymbol{\beta})$ to be the convolution of the filter function with the observed all-sky map at frequency ν ,

$$u_\nu(R_\nu, \boldsymbol{\beta}) = \int d\Omega s_\nu(\boldsymbol{\theta}) \psi_\nu(|\boldsymbol{\theta} - \boldsymbol{\beta}|, R_\nu) \quad (38)$$

$$= \sum_{\ell=0}^{\infty} \sum_{m=-\ell}^{+\ell} u_{\ell m, \nu} Y_\ell^m(\boldsymbol{\beta}) \text{ with} \quad (39)$$

$$u_{\ell m, \nu} = \sqrt{\frac{4\pi}{2\ell + 1}} s_{\ell m, \nu} \psi_{\ell 0, \nu}(R_\nu). \quad (40)$$

For the second step, the convolution theorem to be derived in Appendix A was used. The combined filtered field is defined by

$$u(R_1, \dots, R_N; \beta) = \sum_v u_v(R_v, \beta). \quad (41)$$

Taking into account the vanishing expectation value of the noise $\langle n_v(\theta) \rangle = 0$, the expectation value of the filtered field at the North pole $\beta = \mathbf{0}$ is given by

$$\langle u_v(R_v, \mathbf{0}) \rangle = A f_v \sum_{\ell=0}^{\infty} \tau_{\ell 0, v} \psi_{\ell 0, v}(R_v). \quad (42)$$

The assumption that the cross power spectrum of the signal is negligible compared to the noise power spectrum is justified because the thermal and kinetic amplitudes are small compared to unity, $A_{y,w} \ll 1$. Thus, the variance of the combined filtered field (41) is determined by

$$\begin{aligned} \sigma_u^2(R_1, \dots, R_N) &= \langle [u(R_1, \dots, R_N; \beta) - \langle u(R_1, \dots, R_N; \beta) \rangle]^2 \rangle \\ &= \sum_{v_1, v_2} \sum_{\ell} C_{\ell, v_1 v_2} \psi_{\ell 0, v_1}(R_{v_1}) \psi_{\ell 0, v_2}(R_{v_2}). \end{aligned} \quad (43)$$

The optimised filter functions $\psi_v(\theta)$ are chosen to detect the clusters at the North pole of the sphere (to which they have been translated). They are described by a singly peaked profile which is characterised by the scale $R_v^{(0)}$ as given by eqn. (35). While the optimised *matched filter* is defined to obey the first two of the following conditions, the optimised *scale-adaptive filter* is required to obey all three conditions:

- (i) The combined filtered field $u(R_1^{(0)}, \dots, R_N^{(0)}; \mathbf{0})$ is an unbiased estimator of the source amplitude A , i.e. $\langle u(R_1^{(0)}, \dots, R_N^{(0)}; \mathbf{0}) \rangle = A$.
- (ii) The variance of $u(R_1, \dots, R_N; \beta)$ has a minimum at the scales $R_1^{(0)}, \dots, R_N^{(0)}$ ensuring that the combined filtered field is an efficient estimator.
- (iii) The expectation value of the filtered field at the source position has an extremum with respect to the the scale $R_v^{(0)}$, implying

$$\frac{\partial}{\partial R_v^{(0)}} \langle u_v(R_v, \mathbf{0}) \rangle = 0. \quad (44)$$

6.3 Matched filter

For convenience, we introduce the column vectors $\psi_\ell \equiv [\psi_{\ell 0, v}]$, $\mathbf{F}_\ell \equiv [f_v \tau_{\ell 0, v}]$, and the inverse $\hat{\mathbf{C}}_\ell^{-1}$ of the matrix $\hat{\mathbf{C}}_\ell \equiv [C_{\ell, v_1 v_2}]$. In terms of spherical harmonic expansion coefficients, constraint (i) reads

$$\sum_v \sum_{\ell=0}^{\infty} f_v \tau_{\ell 0, v} \psi_{\ell 0, v} = \sum_{\ell=0}^{\infty} \mathbf{F}_\ell^T \hat{\mathbf{C}}_\ell^{-1} \mathbf{F}_\ell = 1. \quad (45)$$

Performing functional variation (with respect to the filter function ψ_ℓ) of $\sigma_u^2(R_1, \dots, R_N)$ while incorporating the (isoperimetric) boundary condition (45) through a Lagrangian multiplier yields the spherical matched filter ψ_ℓ

$$\psi_\ell = \alpha \hat{\mathbf{C}}_\ell^{-1} \mathbf{F}_\ell, \quad \text{where} \quad \alpha^{-1} = \sum_{\ell=0}^{\infty} \mathbf{F}_\ell^T \hat{\mathbf{C}}_\ell^{-1} \mathbf{F}_\ell. \quad (46)$$

In any realistic application, the cross power spectrum $C_{\ell, v_1 v_2}$ can be computed from observed data provided the cross power spectrum of the signal is negligible. The quantities α , $\mathbf{F}_{\ell 0}$, and thus $\psi_{\ell 0}$ can be computed in a straightforward manner for a specific frequency dependence f_v and for a model source profile $\tau_v(\theta)$.

6.4 Scale-adaptive filter on the sphere

The scale-adaptive filter ψ_ℓ satisfying all three conditions is given by

$$\psi_\ell = \hat{\mathbf{C}}_\ell^{-1} (\alpha \mathbf{F}_\ell + \mathbf{G}_\ell), \quad \text{with} \quad \mathbf{G}_\ell \equiv [\mu_{\ell, v} \beta_v], \quad \text{and} \quad (47)$$

$$\mu_{\ell, v} \equiv f_v \tau_{\ell 0, v} \left(2 + \frac{d \ln \tau_{\ell 0, v}}{d \ln \ell} \right) = f_v [2 \tau_{\ell 0, v} + \ell (\tau_{\ell 0, v} - \tau_{\ell-1 0, v})]. \quad (48)$$

As motivated in Appendix A5, the logarithmic derivative of $\tau_{\ell 0}$ with respect to the multipole order ℓ is a shorthand notation of the differential quotient which is only valid for $\ell \gg 1$. The quantities α and β_v are given by the components

$$\alpha = (\hat{\mathbf{A}}^{-1})_{00}, \quad \beta_v = (\hat{\mathbf{A}}^{-1})_{v0}, \quad (49)$$

where $\hat{\mathbf{A}}$ is the $(1+N) \times (1+N)$ matrix with elements

$$A_{00} \equiv \sum_{\ell=0}^{\infty} \mathbf{F}_\ell^T \hat{\mathbf{C}}_\ell^{-1} \mathbf{F}_\ell, \quad A_{0v} \equiv \sum_{\ell=0}^{\infty} \mu_{\ell, v} (\mathbf{F}_\ell^T \hat{\mathbf{C}}_\ell^{-1})_v, \quad (50)$$

$$A_{v0} \equiv \sum_{\ell=0}^{\infty} \mu_{\ell, v} (\hat{\mathbf{C}}_\ell^{-1} \mathbf{F}_\ell)_v, \quad A_{vv'} \equiv \sum_{\ell=0}^{\infty} \mu_{\ell, v} \mu_{\ell, v'} (\hat{\mathbf{C}}_\ell^{-1})_{vv'} \quad (51)$$

In these equations, no summation over the indices is implied.

6.5 Detection level and gain

As described by Sanz et al. (2001), the concept of constructing an optimised filter function for source detection aims at maximising the signal-to-noise ratio D_u ,

$$D_u \equiv \frac{\langle u(R_1, \dots, R_N; \mathbf{0}) \rangle}{\sigma_u(R_1, \dots, R_N)} = A \cdot \frac{\sum_{\ell=0}^{\infty} \mathbf{F}_\ell^T \psi_\ell}{\sqrt{\sum_{\ell=0}^{\infty} \psi_\ell^T \hat{\mathbf{C}}_\ell \psi_\ell}}. \quad (52)$$

Computing the dispersion of the unfiltered field on the sphere yields the signal-to-noise ratio D_s of a signal on the fluctuating background:

$$\sigma_s^2 = \sum_{v_1, v_2} \sum_{\ell=0}^{\infty} C_{\ell, v_1 v_2} \Rightarrow D_s = \frac{A}{\sigma_s}. \quad (53)$$

These considerations allow introducing the *gain* for comparing the signal-to-noise ratios of a peak before and after convolution with a filter function:

$$g \equiv \frac{D_u}{D_s} = \frac{\sigma_s}{\sigma_u(R_1, \dots, R_N)}. \quad (54)$$

If the noise suppression is successful, the gain g will assume values larger than one. If the filters are constructed efficiently, they are able to reduce the dispersion ($\sigma_u(R_1, \dots, R_N) < \sigma_s$) while simultaneously retaining the expectation value of the field (42). Due to the additional third constraint, the scale-adaptive filter is expected to achieve smaller gains compared to the matched filter.

6.6 Numerical derivation of filter kernels

For the derivation of suitable filter kernels the source profiles are assumed to be generalised King-profiles as described by eqn. (36) convolved with the respective *Planck*-beam superimposed on fluctuating background given by template $\langle S_{\ell m} \rangle_v$ -coefficients. The inversion of the matrix $\hat{\mathbf{C}}_\ell$ (c.f. eqns. (32) and (37)) can be performed using either Gauss-Jordan elimination or LU decomposition, which both were found to yield reliable results. In the derivation of the scale-adaptive filters, however, it is numerically advantageous to

artificially exclude the lower multipoles $\ell \leq 1$ from the calculation. Due to the sub-millimetric emission of the Milky Way, the lower multipoles are very large. Consequently, the corresponding $\psi_{\ell m}$ -coefficients, $\ell \leq 1$, have been set to zero, which is not a serious intervention since the filters are designed to amplify structures at angular scales well below a degree. For consistency, the multipoles below the quadrupole have been artificially removed in the derivation of the matched filters as well.

In contrast to the *Planck*-simulation pipeline all numerical calculations presented here are carried out in terms of fluxes measured in Jy and not in antenna temperatures for the following reason: Cross-power spectra $C_{\ell, \nu_1 \nu_2}$ given in terms of antenna temperatures are proportional to $(\nu_1 \cdot \nu_2)^{-2}$ which results in a suppression of the highest frequency channels by a factor of almost 10^5 compared to the lowest frequency channels.

Furthermore, by working with fluxes instead of antenna temperatures, the filters for extracting the SZ-signal show frequency dependences which can be understood intuitively. The frequency dependence is described by eqns. 29 and 30. The normalisation \mathcal{Y} has been chosen to be 1 arcmin^2 , which corresponds to the weakest signals *Planck* will be able to detect. Because of the smallness of the source profiles to be detected, the calculations were carried out to multipole orders of $\ell_{\text{max}} = 4096$, which ensures that the beams as well as the source profiles are well described. In the plots in Sect. 6.7, the filters depicted are smoothed with a moving average window comprising eleven bins for better visualisation.

6.7 Discussion of filter kernels

6.7.1 Matched filter

The spherical harmonics expansion coefficients $\psi_{\ell 0, \nu}$ following from the matched filter algorithm are depicted in Fig. 15 for four frequencies most relevant to SZ-observation, namely for $\nu = 100 \text{ GHz}$, $\nu = 143 \text{ GHz}$, $\nu = 217 \text{ GHz}$ and $\nu = 353 \text{ GHz}$. As background noise components the clean COS data set (left column) and the exhaustive GAL data set (right column) are contrasted. The filter kernels have been derived for optimised detection of sources described by a generalised King-profile with angular core radii $\theta_c = 3'0$ and $\theta_c = 5'0$ and asymptotic slope $\lambda = 1.0$.

The principle how the matched filter extracts the SZ-signal from the maps is explained by Fig. 15: The SZ-profiles the filter has been optimised are small structures at angular scales corresponding to multipole moments of $\ell \approx 10^3$. In channels below $\nu = 217 \text{ GHz}$, the clusters are observed in absorption and the fluxes are decreased. For that reason, the filters have negative amplitudes at these angular scales for these specific frequencies. At larger scales, the fluctuations are suppressed by linear combination of the various channels, while the filtering functions show very similar shapes. Optimising the filters for detection of core radii of $5'0$ instead of $3'0$ result in a shift of the negative peak at $\ell \approx 10^3$ to smaller multipole orders. Instrumental noise which is important at even higher multipoles is suppressed by the filter's exponential decline at high ℓ above $\ell \gtrsim 2000$. The unwanted CMB fluctuations and all Galactic contributions at scales larger than the cluster scale are suppressed by weightings with varying sign so that the foregrounds are subtracted at the stage of forming linear combinations of the $\langle S_{\ell m} \rangle_{\nu}$ -coefficients.

Furthermore, the contours of the matched filter kernels are given in Fig. 15 as functions of both inverse angular scale ℓ and observing frequency ν for differing noise contributions. The figures compare filters derived for differing background noise com-

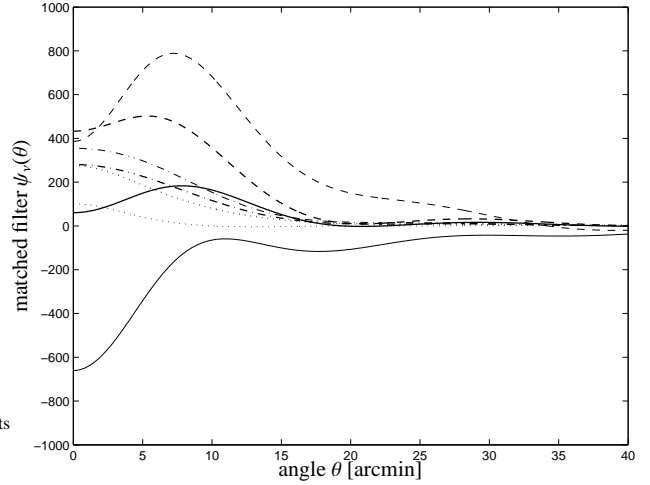


Figure 16. Matched filter kernels $\psi_{\nu}(\theta)$ in real space at SZ-frequencies, i.e. for $\nu = 100 \text{ GHz}$ (solid line), $\nu = 143 \text{ GHz}$ (dashed line), $\nu = 217 \text{ GHz}$ (dotted line) and $\nu = 353 \text{ GHz}$ (dash-dotted line), for a data set including the CMB, Galactic foregrounds and instrumental noise (thin lines) and for a data set containing all Galactic components in addition to the CMB and instrumental noise (thick lines). The filter kernel is optimised for the detection of a generalised King-profile with core radius $\theta_c = 5'0$ and asymptotic slope $\lambda = 1.0$.

positions. The filters shown serve for the optimised detection of generalised King-profiles with core radius $\theta_c = 15'0$ and asymptotic slope $\lambda = 1.0$. These (rather large) values have been chosen for visualisation purposes. For clarity, the contour denoting zero values has been omitted due to noisy data. In these figures it is apparent how the filters combine the frequency information in order to achieve a suppression of the unwanted foregrounds: At multipole moments of a few hundred, the filters exhibit changes in sign, such that the measurements at low frequencies are subtracted from the measurements at high frequencies in the linear combination of the filtered maps.

Fig. 16 illustrates the filter kernels $\psi_{\nu}(\theta)$ in real space for the same selection of frequencies and background noise components as given above. The filter kernels $\psi_{\nu}(\theta)$ have been synthesised from the $\psi_{\ell 0, \nu}$ -coefficients using the *alm2grid*-utility of the *Planck*-simulation package. Here, the parameters of the King-profile to be detected are $(\theta_c, \lambda) = (5'0, 1.0)$. The filter kernels are similar in shape to Mexican-hat wavelets, but show more than one oscillation. Their action on the sky maps is to apply high-pass filtering, such that all long-wavelength modes are eliminated. At the cluster scale, they implement a linear combination of the sky maps that aims at amplifying the SZ-signal: The kernels derived for both the $\nu = 100 \text{ GHz}$ - and $\nu = 143 \text{ GHz}$ -channel exhibit a central depression which is used to convert the SZ-signal to positive amplitudes. The other two channels resemble simple Gaussian kernels which smooth the maps to a common effective angular resolution. At frequencies of $\nu = 217 \text{ GHz}$ and $\nu = 353 \text{ GHz}$ the most important emission feature is Galactic Dust, which is suppressed by the filter's small amplitudes. In this way, the weak SZ-signal is dissected.

In Fig. 17, filter kernels derived with both algorithms for point sources (i.e. with beam profiles of the respective *Planck*-channels) are compared, that have been optimised for the detection of varying spectral behaviour of the signal, in this case the thermal SZ-effect, the kinetic SZ-effect and a Planckian thermal emitter with a surface temperature T_{surface} of 150 K , such as an asteroid or planet.

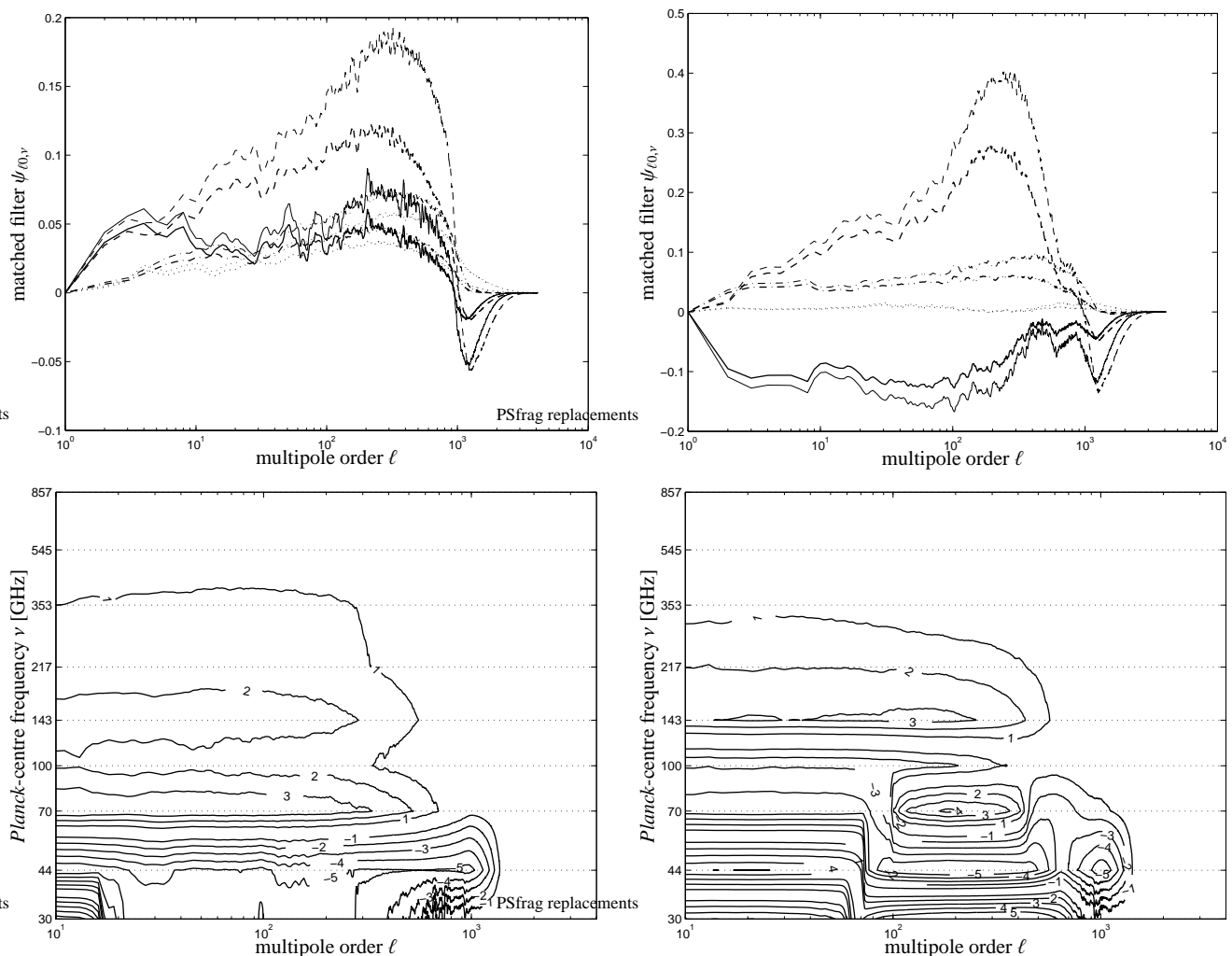


Figure 15. *Upper panel:* Spherical harmonics coefficients $\psi_{\ell 0, \nu}$ as derived with the matched filter algorithm, for $\nu = 100$ GHz (solid line), $\nu = 143$ GHz (dashed line), $\nu = 217$ GHz (dash-dotted line) and $\nu = 353$ GHz (dotted line). The left and right columns compare filter kernels derived for a data set containing only the CMB, the SZ-effects and instrumental noise (left column) and for a data set comprising all Galactic foregrounds in addition (right column). The filter kernels are optimised for the detection of generalised King-profiles with core radii $\theta_c = 3'0$ (thin lines), $\theta_c = 5'0$ (thick lines) and asymptotic slope $\lambda = 1.0$. *Lower panel:* Contour plot of the spherical harmonics expansion coefficients $\psi_{\ell 0, \nu}$ derived with the matched filter algorithm as a function of both the multipole moment order ℓ and Planck's observing frequency ν . The filter kernels have been derived for an optimised detection of a generalised King-profile with $(\theta_c, \lambda) = (15'0, 1.0)$. The contours are linearly spaced in $\text{arsinh}(10^2 \cdot \psi_{\ell 0, \nu})$.

The filter kernels depicted correspond to observing frequencies of $\nu = 143$ GHz and $\nu = 217$ GHz. The filters clearly reflect the spectral behaviour of the emission laws of the sources one aims at detecting: While the filter kernels designed for detecting thermal SZ-clusters reflect the peculiar change in sign in the SZ-effect's frequency dependence, the other two curves show the behaviour to be expected for a Planckian emitter and the kinetic SZ-effect, respectively. Again, the better angular resolution of the $\nu = 217$ GHz-channel is apparent by the shifting of the curves to higher multipole order ℓ .

6.7.2 Scale-adaptive filter

The spherical harmonics expansion coefficients $\psi_{\ell 0, \nu}$ following from the scale-adaptive filter algorithm for the frequencies $\nu = 100$ GHz, $\nu = 143$ GHz, $\nu = 217$ GHz and $\nu = 353$ GHz are given in the upper panel of Fig. 18. The left and right columns com-

pare the filter kernels for differing noise components. Their functional shape has a number of important features in common with the matched filters: They suppress the uncorrelated pixel noise, which is dominant at high ℓ by their exponential decline at $\ell \gtrsim 2000$. Furthermore, the filters amplify the SZ-signal, which is negative at frequencies below $\nu = 217$ GHz, by assuming large negative values and hence converting the SZ-signal to yield positive amplitudes. Additionally, the filters show a distinct secondary peak at $\ell \approx 2000$ which causes the kernels to be more compact after transformation to real space and enables the size measurement. A more general observation is that the scale-adaptive filter kernel shapes are more complex and noisier in comparison to the matched filter, especially at high ℓ .

The scale-adaptive filter makes even stronger use of the spectral information than the matched filter. Especially the contour plots in Fig. 18 show that the scale-adaptive filter exhibits alternating signs when varying the observing frequency ν while keeping the angular scale ℓ fixed. In this way, the noise contributions are iso-

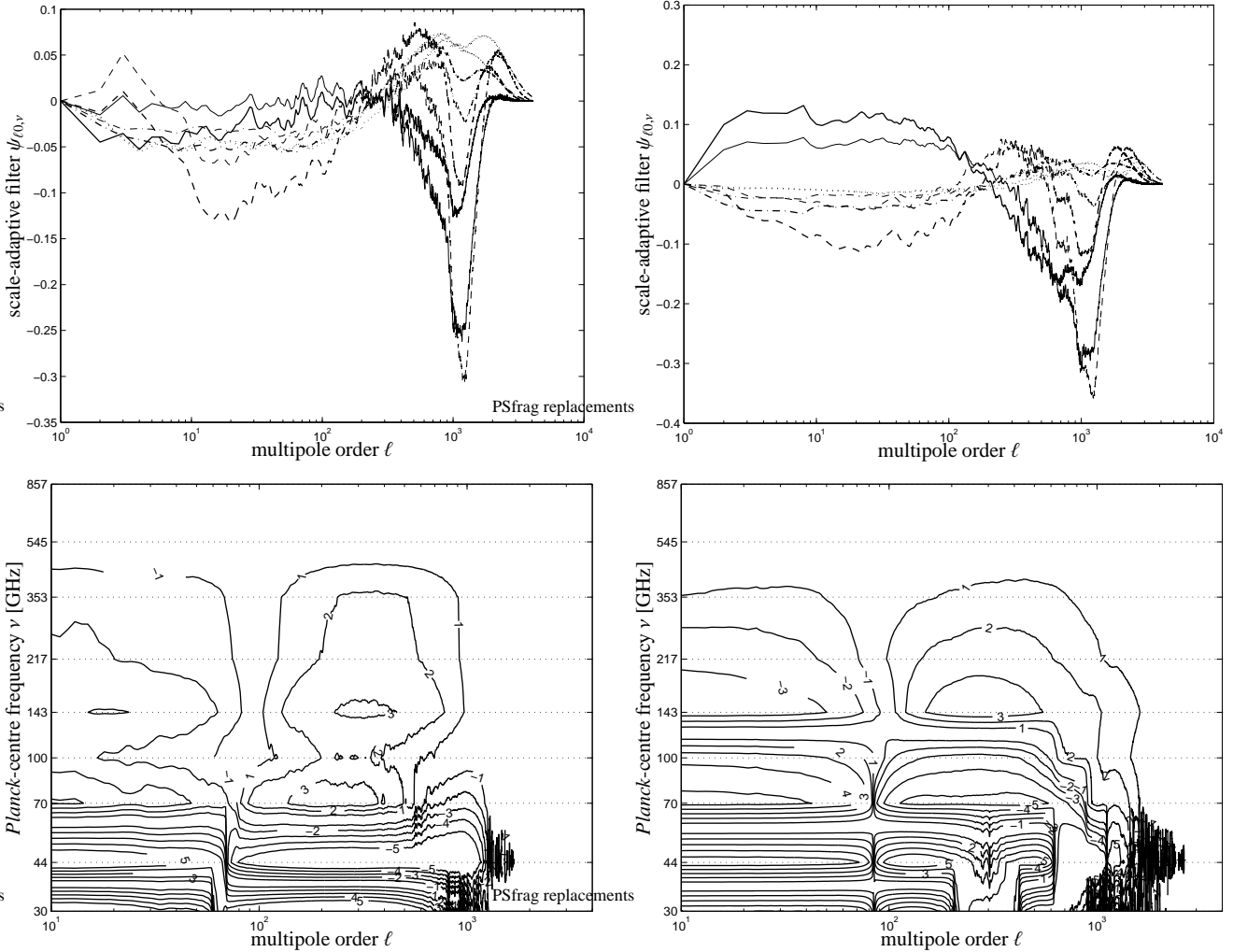


Figure 18. *Upper panel:* Spherical harmonics coefficients $\psi_{\ell 0, \nu}$ as derived with the scale-adaptive filter algorithm, for $\nu = 100$ GHz (solid line), $\nu = 143$ GHz (dashed line), $\nu = 217$ GHz (dash-dotted line) and $\nu = 353$ GHz (dotted line). The filter kernel is optimised for the detection of generalised King-profiles with core radii $\theta_c = 3'.0$ (thin lines) and $\theta_c = 5'.0$ (thick lines) and asymptotic slope $\lambda = 1.0$.

Lower panel: Contour plots of the spherical harmonics expansion coefficients $\psi_{\ell 0, \nu}$ derived with the scale-adaptive filter algorithm as a function of the multipole moment order ℓ and *Planck*'s observing frequency ν are shown. The filter kernels have been derived for an optimised detection of a generalised King-profile with $(\theta_c, \lambda) = (15'.0, 1.0)$. The contours are linearly spaced in $\text{arsinh}(10^2 \cdot \psi_{\ell 0, \nu})$. Again, the columns compare the influence of the fluctuating background, comprising cosmological contributions (CMB and both SZ-effects) and instrumental noise (left column) to the data set that contains all Galactic foregrounds in addition.

lated in angular scale and subsequently suppressed by linear combination of the maps. Furthermore, one notices a change in sign at multipole order $\ell \approx 200$ which is common to the frequencies $\nu = 100 \dots 353$ GHz, at which the CMB signal is strongest. Aiming at reducing the variance of the filtered maps, the scale-adaptive filter is suppressing the $\langle S_{\ell m} \rangle_\nu$ -coefficients by assuming small values.

Fig. 19 gives the filter kernels $\psi_\nu(\theta)$ in real space for selected frequencies and background noise components. The scale-adaptive filters work similarly as the matched filters like Mexican-hat wavelets and subject the sky maps to high pass filtering.

In Fig. 20, filter kernels derived with both algorithms for point sources (i.e. with beam profiles of the respective *Planck*-channels) are compared, that have been optimised for the detection of varying spectral behaviour of the signal, in this case the thermal SZ-effect, the kinetic SZ-effect and a Planckian thermal emitter with a surface temperature T_{surface} of 150 K, such as an asteroid or planet. The

filter kernels depicted correspond to observing frequencies of $\nu = 143$ GHz and $\nu = 217$ GHz. As in the case of the matched filter, the frequency dependence of the signal is reflected by the sign of the filter kernel at the anticipated angular scale of the profile to be detected.

6.8 Filter renormalisation and synthesis of likelihood maps

Once the filter kernels are derived, the filtered fields $u_\nu(R_\nu, \beta)$ can be synthesised from the $u_{\ell m, \nu}$ -coefficients (defined in eqn. (40)) and the resulting maps can be added in order to yield the co-added, filtered field $u(R_1, \dots, R_N, \beta)$ (see eqn. (41)), which can be normalised by the level of fluctuation σ_u (given by eqn. (42)) to yield the likelihood map $D(\theta)$. It is favourable to divide the filter kernels by the variance σ_u and to apply a renormalisation:

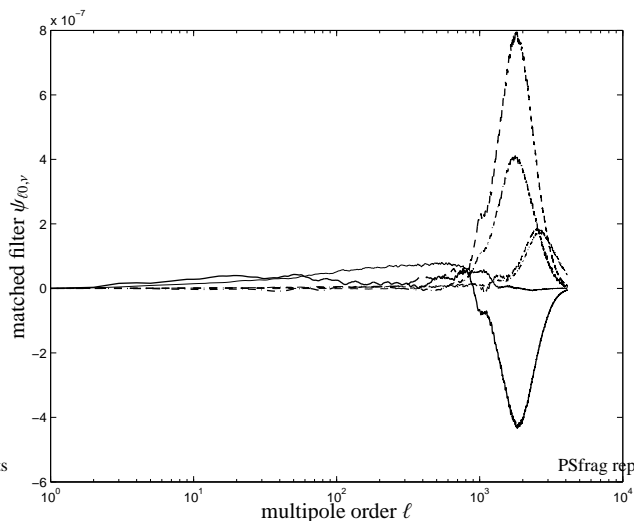


Figure 17. Comparison of filter kernel $\psi_{\ell 0, \nu}$ -coefficients derived for differing spectral dependences of the signal: thermal SZ-effect (solid line), kinetic SZ-effect (dashed line) and a Planckian emitter with surface temperature of $T_{\text{surface}} = 150$ K (dash-dotted line). All sources are assumed to be point-like, i.e. they appear to have the shape of the *Planck*-beam. The curves are given for observing frequencies of $\nu = 143$ GHz (thin line) and $\nu = 217$ GHz (thick line) and have been derived with the matched filter algorithm. The noise is a composite of CMB fluctuations, Galactic and ecliptic foregrounds and instrumental noise.

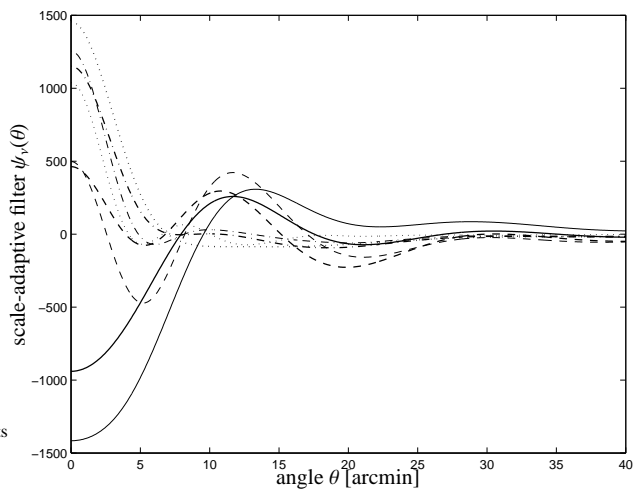


Figure 19. Scale-adaptive filter kernels $\psi_{\nu}(\theta)$ in real space, for $\nu = 100$ GHz (solid line), $\nu = 143$ GHz (dashed line), $\nu = 217$ GHz (dotted line) and $\nu = 353$ GHz (dash-dotted line), for a data set incorporating the CMB, Galactic foregrounds and instrumental noise. The filter kernel is optimised for the detection of a generalised King-profile with parameters $(\theta_c, \lambda) = (5'.0, 1.0)$.

$$\psi_{\ell 0, \nu} \longrightarrow \psi'_{\ell 0, \nu} = \frac{\psi_{\ell 0, \nu}}{\sqrt{\sum_{\ell} \psi_{\ell}^T \hat{C}_{\ell} \psi_{\ell}}} \quad (55)$$

In this case, the filter kernels are invariant under changes in profile normalisation. With these kernels, the filtered flux maps can be synthesised from the set of $\langle S_{\ell m} \rangle_{\nu}$ -coefficients and the resulting maps can be co-added to yield the final normalised likelihood map $D(\beta)$. It is computationally advantageous, however, to interchange

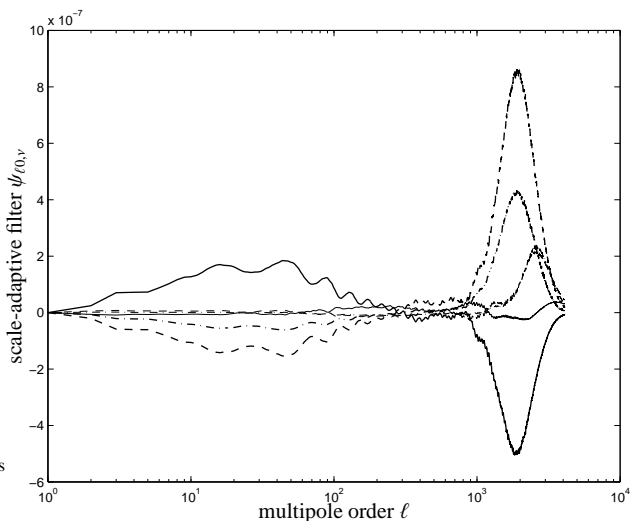


Figure 20. Comparison of filter kernel $\psi_{\ell 0, \nu}$ -coefficients derived for differing spectral dependences of the signal: thermal SZ-effect (solid line), kinetic SZ-effect (dashed line) and a Planckian emitter with surface temperature of $T_{\text{surface}} = 150$ K (dash-dotted line). All sources are assumed to be point-like, i.e. they appear to have the shape as the *Planck*-beam. The curves are given for observing frequencies of $\nu = 143$ GHz (thin line) and $\nu = 217$ GHz (thick line) and have been derived with the scale-adaptive filter algorithm. The noise is a composite of CMB fluctuations, Galactic and ecliptic foregrounds and instrumental noise.

the last two steps,

$$D_u(\beta) = \frac{u(\beta)}{\sigma_u} = \frac{1}{\sigma_u} \sum_{\nu} u_{\nu}(\beta) \quad (56)$$

$$= \sum_{\nu} \sum_{\ell=0}^{\infty} \sum_{m=-\ell}^{+\ell} \sqrt{\frac{4\pi}{2\ell+1}} \langle S_{\ell m} \rangle_{\nu} \frac{\psi_{\ell 0, \nu}}{\sqrt{\sum_{\ell} \psi_{\ell}^T \hat{C}_{\ell} \psi_{\ell}}} Y_{\ell}^m(\beta) \quad (57)$$

$$= \sum_{\ell=0}^{\infty} \sum_{m=-\ell}^{+\ell} \underbrace{\sqrt{\frac{4\pi}{2\ell+1}} \left[\sum_{\nu} \langle S_{\ell m} \rangle_{\nu} \cdot \psi'_{\ell 0, \nu} \right]}_{\equiv D_{\ell m}} Y_{\ell}^m(\beta), \quad (58)$$

and to derive the $D_{\ell m}$ -coefficients first, such that the synthesis has to be performed only once. Due to the restriction to axially symmetric kernels, the convolution can be carried out using the `alm2map` utility rather than `totalconvolve`.

Fig. 21 gives a visual impression of the capability of the above described filtering schemes: The figure shows a $30^{\circ} \times 30^{\circ}$ wide field at the ecliptic North pole at a frequency of $\nu = 353$ GHz (at the SZ-maximum) as observed by *Planck*, i.e. the image is smoothed to an angular resolution of $\Delta\theta = 5'.0$ (FWHM) and contains the fluctuating CMB, all Galactic and ecliptic foregrounds as well as pixel noise. Matched and scale-adaptive filter kernels were derived for isolating point sources, i.e. for sources that appear to have profiles equal to *Planck*'s beams of the corresponding channel. For clarity, only amplitudes exceeding a threshold value of 1.0 are shown.

For comparison, Fig. 21 shows the same detail of the input thermal SZ-map as well. It is immediately apparent that the observation of SZ-clusters without foreground- and noise suppression is not possible and that one has to rely on filtering schemes. As a comparison with Fig. 21 shows, the filters are clearly able to isolate the SZ-clusters and to strongly suppress all spurious noise contributions. The matched filter, however, shows a slightly better performance and yields more significant peaks due to better background

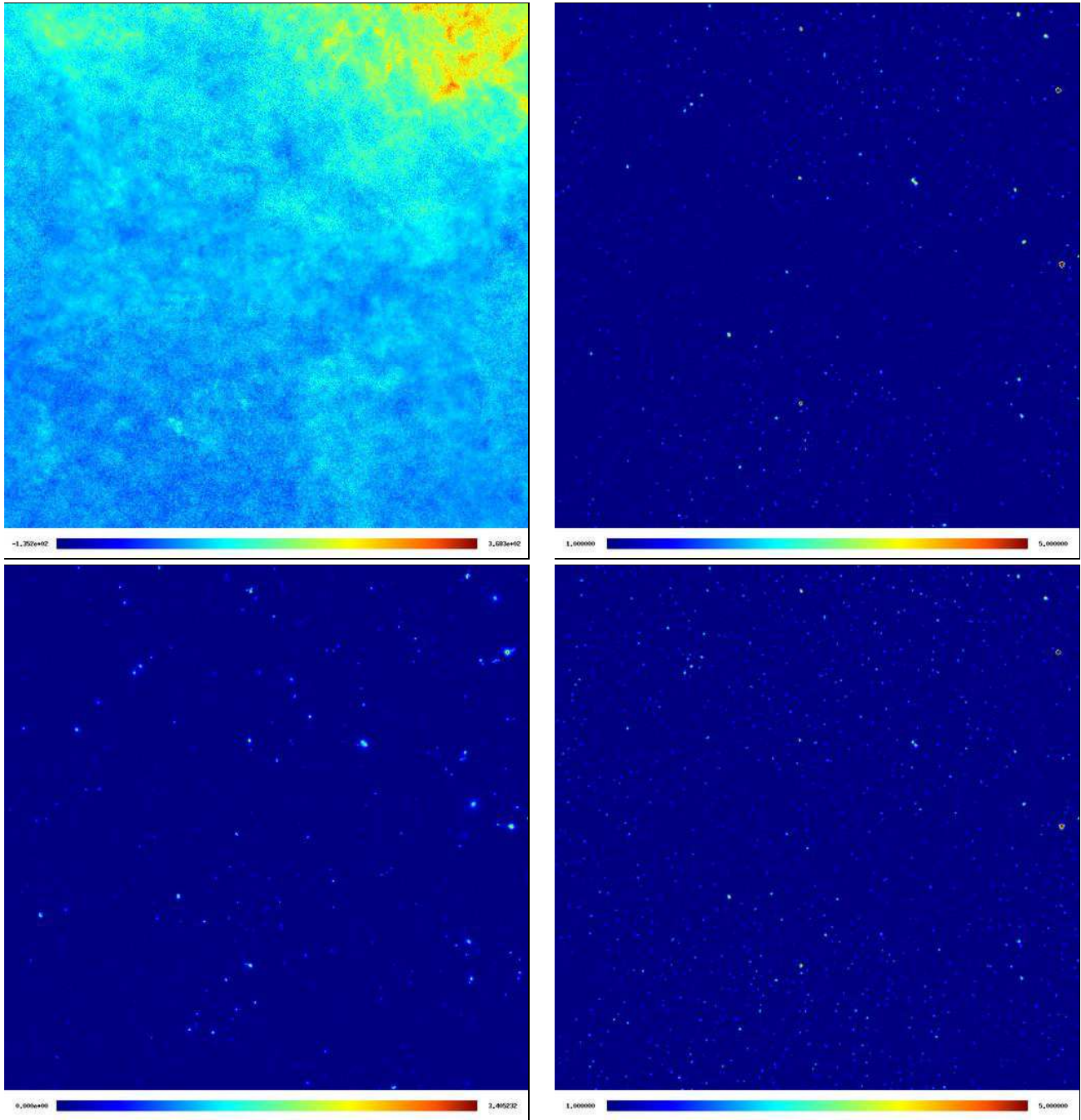


Figure 21. *Upper left panel:* A $30^\circ \times 30^\circ$ wide field centered on the ecliptic North pole as synthesised from a data set containing the CMB, all Galactic and ecliptic foregrounds and instrumental noise for an observing frequency of $\nu = 353$ GHz is shown. The amplitudes are proportional to $\text{arsinh}(T_A(\nu = 353 \text{ GHz})/\mu\text{K})$ and the field is smoothed with the corresponding *Planck*-beam of $\Delta\theta = 5'.0$ (FWHM). *Upper right panel:* The same field is shown after reconstruction from the $D_{\ell m}$ -coefficients. Here, filters derived with the matched filter algorithm optimised for detecting point sources were employed. The amplitudes are given in detection significances and the shading scales linearly. *Lower right panel:* Again, the same field is shown after synthesis from the $D_{\ell m}$ -coefficients but in this case, filters derived with the scale-adaptive filter algorithm optimised for detecting point sources were used. The amplitudes are stated as detection significances and the shading is linear. In the *lower left panel*, the corresponding field taken from the original thermal SZ-map is given for comparison. The amplitudes are $\propto \text{arsinh}(10^4 \cdot y)$.

suppression. There are weak residuals present in both maps due to incomplete foreground reduction. These residuals however, have small amplitudes compared to the SZ-detections. The highest peaks exhibit detection significances amounting to 10.6σ in the case of the matched filter and 9.1σ in the case of the scale-adaptive filter.

It should be emphasised that the filters work exceptionally well despite the fact that the Milky Way clearly is a non-Gaussian feature, whereas Gaussianity of the fluctuating background was an important assumption in the derivation of the filter kernels. Furthermore, the filters successfully separate and amplify the weak SZ-signal in the presence of seven different noise contributions (CMB,

four Galactic foregrounds, thermal emission from bodies of the Solar system and instrumental noise) that exhibit different spectral behaviours by relying on just nine broad-band measurements. Fig. 22 summarises all steps involved in the simulation of *Planck*-observations, filter derivation and signal extraction.

7 SUMMARY AND CONCLUSION

A simulation for assessing *Planck*'s SZ-capabilities in the presence of spurious signals is presented that combines maps of the thermal and kinetic SZ-effects with a realisation of the cosmic microwave background (CMB), in addition to Galactic foregrounds (synchrotron emission, free-free emission, thermal emission from dust, CO-line radiation) as well as the sub-millimetric emission from celestial bodies of our Solar system. Additionally, observational issues such as the finite angular resolution and spatially non-uniform instrumental noise of *Planck* are taken into account.

- Templates for modelling the free-free emission and the carbon monoxide-line emission have been added to the *Planck*-simulation pipeline. The free-free template relies on an H_α -survey of the Milky Way. The spectral properties of both foregrounds are modelled with reasonable parameter choices, i.e. $T_p = 10^4$ K for the free-free plasma temperature and $T_{CO} = 20$ K for the mean temperature of giant molecular clouds.

- An extensive package for modelling the sub-millimetric emission from planet and asteroids has been implemented for *Planck*, that solves the heat balance equation of each celestial body. It takes the movement of the planets and asteroids into account, which causes, due to *Planck*'s scanning strategy, double detections separated by approximate half-year intervals. The total number of asteroids implemented is $\simeq 1200$.

- The foregrounds have been combined under proper inclusion of *Planck*'s frequency response windows in order to yield a set of flux maps. The auto- and cross-correlation properties of those maps are investigated in detail. Furthermore, their decomposition into spherical harmonics $\langle S_{\ell m} \rangle_\nu$ serve as the basis for the filter construction. It should be emphasised that the spectral properties of a foreground component were assumed to be isotropic.

- In order to separate the SZ-Signal and to suppress the foreground components, the theory of matched and scale-adaptive filtering has been extended to spherical data sets. The formulae in the context of spherical coordinates and Y_ℓ^m -decomposition are analogous to those derived for Cartesian coordinate systems and Fourier-transforms.

- The global properties of filter kernel shapes are examined as functions of observing channel, composition of noise, parameters of the profile to be detected and spectral dependence of the signal. Transformation of the filter kernels to real space yields functions that resemble the Mexican-hat wavelets, but show more than one oscillation. The shape of the filter kernels can be understood intuitively: They subject the maps to high-pass filtering while retaining structures similar in angular extent to the predefined profile size. The signal is then amplified by linear combination of the maps, which again is apparent in the sign of the filter kernels.

- The functionality of the filtering scheme is verified by applying them to simulated observations. It is found that the Galactic foregrounds can be suppressed very effectively so that the SZ-cluster signals can be retrieved. Comparing the two filters, the scale-adaptive filter performs not as good as the matched filter, which is in accordance to the findings of Herranz et al. (2002a,b). It should be emphasised that for the derivation of the filter kernels

nothing but a model profile and all cross-power spectra (in *Planck*'s case a total number of 45 independent $C_{\ell,\nu_1\nu_2}$ -sets) are used.

The scientific exploitation of our simulation and the characterisation of *Planck*'s SZ-cluster sample, e.g. the number density as a function of detection significance as well as filter parameters, spatial distribution in dependence on Galactic and ecliptic latitude and the distribution in redshift, mass and apparent size will be the subject of a forthcoming paper.

ACKNOWLEDGEMENTS

The authors would like to thank Torsten Enßlin for careful reading of the manuscript. The support provided by Martin Reinecke in enhancing the *Planck*-simulation tools and adding custom changes is greatly appreciated.

APPENDIX A: OPTIMISED FILTER FOR SINGLE FREQUENCY ALL-SKY OBSERVATIONS

This appendix derives the optimised filters for single frequency all-sky observations and thus serves as a detailed supplement to Sect. 6 where optimised filters for multi-frequency observations were derived. The formalism outlined in this appendix might be applied to future all-sky surveys in the X-ray or microwave regime.

A1 Assumptions and definitions

In order to construct our filters, we consider an all-sky map of the detected scalar field $s(\boldsymbol{\theta})$

$$s(\boldsymbol{\theta}) = y(|\boldsymbol{\theta} - \boldsymbol{\theta}_0|) + n(\boldsymbol{\theta}), \quad (\text{A1})$$

where $\boldsymbol{\theta} = (\vartheta, \varphi)$ denotes a two-dimensional vector on the sphere and $\boldsymbol{\theta}_0$ is the source location. The first term of the right-hand side represents the amplitude of the sources to be detected, while the second term in corresponds to the generalised noise present in the map which is composed of any detected features other than the desired signal including for instance instrumental noise. The statistical properties of the noise are assumed to be characterised by its power spectrum $\langle n_{\ell m} n_{\ell' m'}^* \rangle = C_\ell \delta_{\ell\ell'} \delta_{mm'}$. In order to sketch the construction of the optimised filter, we assume an individual cluster situated at the North pole ($\boldsymbol{\theta}_0 = \mathbf{0}$) with a characteristic angular SZ-signal $y(\theta = |\boldsymbol{\theta}|) = A\tau(\theta)$, separating the amplitude A and the profile $\tau(\theta)$.

A2 Convolution theorem on the sphere

Filtering a scalar field on the sphere with an arbitrary, asymmetric kernel requires the specification of the convolution path as well as the orientation of the filter kernel at each position on the sphere in order to apply any convolution algorithm (Wandelt & Górski 2001). Because of the simplifying restriction to centrally symmetric filter kernels, we give the theorem for the convolution of two functions, one of which is assumed to be centrally symmetric. The filtered field $u(\boldsymbol{\beta})$ is obtained by convolution of the centrally symmetric filter function $\psi(\boldsymbol{\theta})$ with the scalar field on the sphere $s(\boldsymbol{\theta})$,

$$u(\boldsymbol{\beta}) = \int d\Omega s(\boldsymbol{\theta}) \psi(|\boldsymbol{\theta} - \boldsymbol{\beta}|). \quad (\text{A2})$$

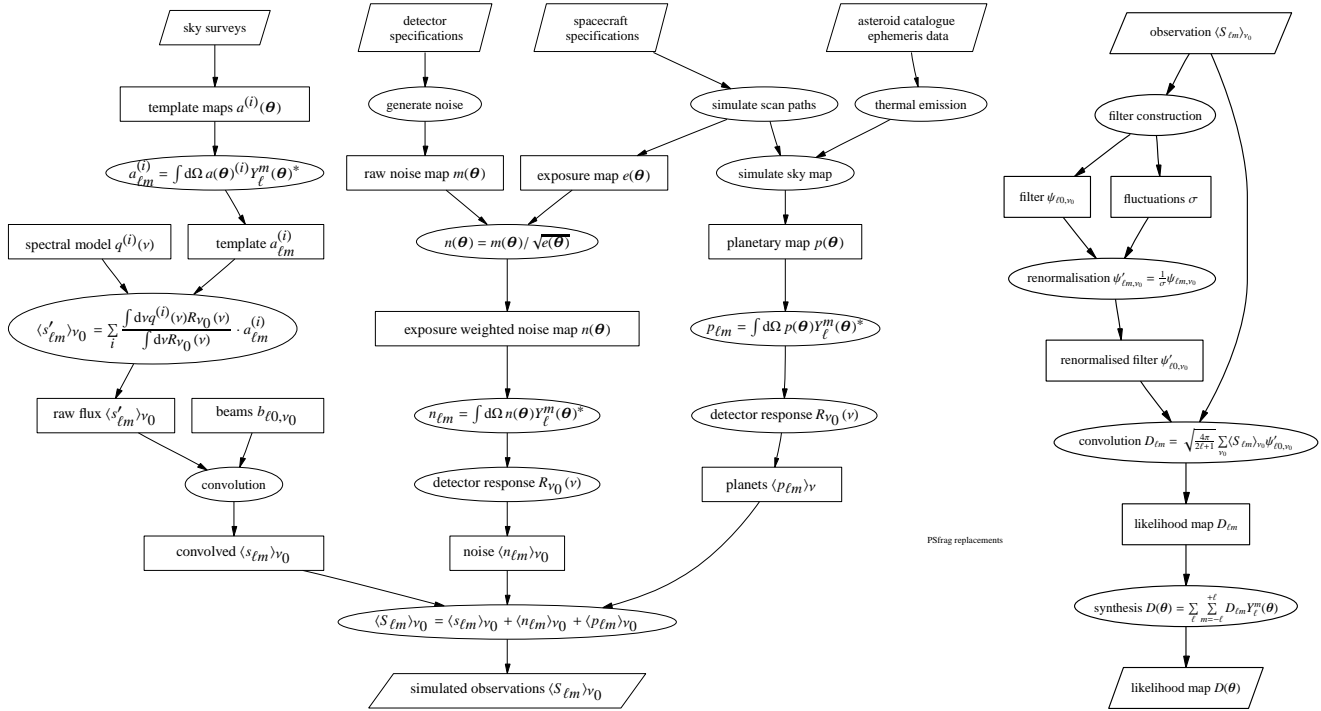


Figure 22. Flow chart summarising all steps involved in the simulation of *Planck*-observations and the derivation of $\langle S_{\ell m} \rangle_{\nu_0}$ -coefficients (left panel) and in the filter construction and signal extraction (right panel).

Expansion of these two scalar fields into spherical harmonics yields

$$s(\theta) = \sum_{\ell=0}^{\infty} \sum_{m=-\ell}^{+\ell} s_{\ell m} Y_{\ell}^m(\theta), \quad (\text{A3})$$

$$\psi(\theta) = \sum_{\ell=0}^{\infty} \sum_{m=-\ell}^{+\ell} \psi_{\ell m} Y_{\ell}^m(\theta) = \sum_{\ell=0}^{\infty} \sqrt{\frac{2\ell+1}{4\pi}} \psi_{\ell 0} P_{\ell}(\cos \theta). \quad (\text{A4})$$

The last step assumes central symmetry. In this case, only modes with $m = 0$ are contributing. For proceeding, the addition theorem for Legendre polynomials $P_{\ell}(x)$ (Arfken & Weber 1995) is used in substituting $\gamma = |\theta - \beta|$:

$$P_{\ell}(\cos \gamma) = \frac{4\pi}{2\ell+1} \sum_{m=-\ell}^{+\ell} Y_{\ell}^m(\theta) Y_{\ell}^{m*}(\beta). \quad (\text{A5})$$

Combining these equations and applying the completeness relation yields the convolution relation for a centrally symmetric filter kernel,

$$u(\beta) = \sum_{\ell=0}^{\infty} \sum_{m=-\ell}^{+\ell} u_{\ell m} Y_{\ell}^m(\beta), \quad \text{with } u_{\ell m} = \sqrt{\frac{4\pi}{2\ell+1}} s_{\ell m} \psi_{\ell 0}. \quad (\text{A6})$$

A3 Concepts of optimised filtering on the sphere

The idea of optimised matched filters was proposed by Tegmark & de Oliveira-Costa (1998), and generalised to scale-adaptive filters by Sanz et al. (2001) for a flat topology. The construction of a centrally symmetric optimised filter function $\psi(\theta)$ for the amplification and detection of signal profiles differing only in size but not in shape implies a family of filters $\psi(\theta/R)$ introducing a scaling parameter R . Decomposing the family of filter functions $\psi(\theta/R)$ into spherical harmonics yields

$$\psi\left(\frac{\theta}{R}\right) = R^2 \sum_{\ell=0}^{\infty} \sqrt{\frac{2\ell+1}{4\pi}} \psi_{\ell 0}(R) P_{\ell}(\cos \theta), \quad (\text{A7})$$

$$\psi_{\ell 0}(R) = \frac{1}{R^2} \int d^2\theta \sqrt{\frac{2\ell+1}{4\pi}} \psi\left(\frac{\theta}{R}\right) P_{\ell}(\cos \theta), \quad (\text{A8})$$

while allowing for central symmetry of the filter function. For a particular choice of R the filtered field $u(R, \beta)$ is obtained by convolution (c.f. Appendix. A2):

$$u(R, \beta) = \sum_{\ell=0}^{\infty} \sum_{m=-\ell}^{+\ell} u_{\ell m} Y_{\ell}^m(\beta), \quad \text{and} \quad (\text{A9})$$

$$u_{\ell m} = \sqrt{\frac{4\pi}{2\ell+1}} s_{\ell m} \psi_{\ell 0}(R). \quad (\text{A10})$$

Taking into account the vanishing expectation value of the noise $\langle n_{\nu}(\theta) \rangle = 0$, the expectation value of the filtered field at the North pole $\beta = \mathbf{0}$ is given by

$$\langle u(R, \mathbf{0}) \rangle = A \sum_{\ell=0}^{\infty} \tau_{\ell 0} \psi_{\ell 0}(R). \quad (\text{A11})$$

Assuming that the power spectrum of the signal is negligible compared to the noise power spectrum, the variance of the filtered field is given by

$$\sigma_u^2(R) = \langle [u(R, \beta) - \langle u(R, \beta) \rangle]^2 \rangle = \sum_{\ell=0}^{\infty} C_{\ell} \psi_{\ell 0}^2(R). \quad (\text{A12})$$

While the optimised *matched filter* in the case of single frequency observations is defined to obey the first two of the following conditions, the optimised *scale-adaptive filter* is required to obey all three conditions:

(i) The filtered field $u(R, \mathbf{0})$ is an unbiased estimator of the source amplitude A at the true source position, i.e. $\langle u(R, \mathbf{0}) \rangle = A$.

(ii) The variance of $u(R, \beta)$ has a minimum at the scale R ensuring that the filtered field is an efficient estimator.

(iii) The expectation value of the filtered field at the source position has an extremum with respect to the the scale R , implying

$$\frac{\partial}{\partial R} \langle u(R, \mathbf{0}) \rangle = 0. \quad (\text{A13})$$

A4 Matched filter

In order to derive the matched filter, constraint (i) can be rewritten yielding

$$\sum_{\ell=0}^{\infty} \tau_{\ell 0} \psi_{\ell 0} = 1. \quad (\text{A14})$$

Performing functional variation (with respect to the filter function ψ) of $\sigma_u^2(R)$ while incorporating the constraint (A14) through a Lagrangian multiplier yields the spherical matched filter:

$$\psi_{\ell 0} = \alpha \frac{\tau_{\ell 0}}{C_{\ell}}, \quad \text{where} \quad \alpha^{-1} = \sum_{\ell=0}^{\infty} \frac{\tau_{\ell 0}^2}{C_{\ell}}. \quad (\text{A15})$$

In any realistic application, the power spectrum C_{ℓ} can be estimated from the observed data provided the power spectrum of the signal is negligible. The quantities α , $\tau_{\ell 0}$, and thus the filter kernel $\psi_{\ell 0}$ can be straightforwardly computed for any model source profile $\tau(\theta)$.

A5 Scale-adaptive filter

The next step consists of reformulating constraint (iii) in order to find a convenient representation for the application of functional variation. The expansion coefficient of the family of filter functions $\psi(\theta/R)$ of eqn. (A7) can be rewritten yielding

$$\psi_{\ell 0}(R) = \frac{1}{R^2} \int d^2\theta \psi\left(\frac{\theta}{R}\right) Y_{\ell}^0(\theta) = \int d^2\beta \psi(\beta) Y_{\ell}^0(R\beta), \quad (\text{A16})$$

where $\beta \equiv \theta/R$. In general, this substitution is *not* valid, because $d^2\theta = \sin\theta d\theta d\phi$. In the case of localised source profiles, the angle θ is small for non-vanishing values of ψ justifying the approximation $\sin\theta \approx \theta$. The same argument also applies for the boundaries of integration. With the aid of eqn. (A11), condition (A13) reads

$$\frac{\partial}{\partial R} \langle u(R, \mathbf{0}) \rangle = \sum_{\ell=0}^{\infty} \tau_{\ell 0} \frac{\partial \psi_{\ell 0}(R)}{\partial R} = 0. \quad (\text{A17})$$

Using eqn. (A16), the derivative now acts on the Legendre polynomial P_{ℓ} ,

$$\sum_{\ell=0}^{\infty} \sqrt{\frac{2\ell+1}{4\pi}} \tau_{\ell 0} \int d^2\beta \psi(\beta) P'_{\ell}(\cos R\beta) \beta \sin R\beta = 0. \quad (\text{A18})$$

Using the derivative relation of the Legendre polynomials (Arfken & Weber 1995),

$$P'_{\ell}(x) = \frac{\ell+1}{1-x^2} [x P_{\ell}(x) - P_{\ell+1}(x)], \quad (\text{A19})$$

one obtains

$$\sum_{\ell=0}^{\infty} \sqrt{\frac{2\ell+1}{4\pi}} (\ell+1) \tau_{\ell 0} \int d^2\beta \psi(\beta) \frac{R\beta}{\sin R\beta} \times [\cos R\beta P_{\ell}(\cos R\beta) - P_{\ell+1}(\cos R\beta)] = 0. \quad (\text{A20})$$

In our case, the angle θ is small for non-vanishing values of ψ justifying the approximations $\sin R\beta \approx R\beta$ and $\cos R\beta \approx 1$. Substituting back, $d^2\beta = d^2\theta/R^2$, introducing $x \equiv \cos\theta = \cos R\beta$, and inserting the inversion of eqn. (A16), namely

$$\psi(\beta) = \sum_{\ell'=0}^{\infty} \psi_{\ell'0}(R) Y_{\ell'0}^0(R\beta), \quad (\text{A21})$$

one arrives at

$$\sum_{\ell', \ell=0}^{\infty} \sqrt{\frac{2\ell+1}{4\pi}} \sqrt{\frac{2\ell'+1}{4\pi}} (\ell+1) \tau_{\ell 0} \psi_{\ell'0}(R) \times \frac{2\pi}{R^2} \int dx P_{\ell}(x) [P_{\ell}(x) - P_{\ell+1}(x)] = 0. \quad (\text{A22})$$

Applying the orthogonality relation for the Legendre polynomials,

$$\int_{-1}^{+1} dx P_{\ell}(x) P_{\ell'}(x) = \frac{2}{2\ell+1} \delta_{\ell\ell'}, \quad (\text{A23})$$

and using the small angle approximation in the second term of eqn. (A22) with the same argument as given above, yields the final result

$$\sum_{\ell=0}^{\infty} \psi_{\ell 0}(R) [\tau_{\ell 0} + \ell(\tau_{\ell 0} - \tau_{\ell-1,0})] = 0. \quad (\text{A24})$$

Replacing the differential quotient with the corresponding derivative is a valid approximation for $\ell \gg 1$. Thus, eqn. (A24) can be recast in shorthand notation yielding

$$\sum_{\ell=0}^{\infty} \psi_{\ell 0}(R) \tau_{\ell 0} \left[2 + \frac{d \ln \tau_{\ell 0}}{d \ln \ell} \right] = 0. \quad (\text{A25})$$

This result could have been obtained independently by attaching the tangential plane to the North pole and applying Fourier decomposition of the filter function ψ and the source profile τ . For that reason, it is not surprising that the functional form of this condition on the sphere agrees with that obtained by Sanz et al. (2001) for a flat topology in two dimensions.

Performing functional variation (with respect to the filter function ψ) of $\sigma_u^2(R)$ while interlacing the constraints (A14) and (A25) through a pair of Lagrangian multipliers yields the spherical scale-adaptive filter,

$$\psi_{\ell 0} = \frac{\tau_{\ell 0}}{C_{\ell} \Delta} \left[2b + c - (2a + b) \frac{d \ln \tau_{\ell 0}}{d \ln \ell} \right], \quad (\text{A26})$$

$$\Delta = ac - b^2,$$

$$a = \sum_{\ell=0}^{\infty} \frac{\tau_{\ell 0}^2}{C_{\ell}}, \quad b = \sum_{\ell=0}^{\infty} \frac{\tau_{\ell 0}}{C_{\ell}} \frac{d \tau_{\ell 0}}{d \ell},$$

$$c = \sum_{\ell=0}^{\infty} C_{\ell}^{-1} \left(\frac{d \tau_{\ell 0}}{d \ln \ell} \right)^2. \quad (\text{A27})$$

As before in the case of the matched filter, the power spectrum C_{ℓ} can be derived from observed data provided the power spectrum of the signal is negligible. Assuming a model source profile $\tau(\theta)$, the quantities $\tau_{\ell 0}$, a , b , c , and finally $\psi_{\ell 0}$ can be computed in a straightforward way. The derivative of $\tau_{\ell 0}$ with respect to the multiple order ℓ is a shorthand notation of the differential quotient in eqn. (A24).

REFERENCES

Aghanim N., Hansen S. H., Lagache G., 2004, ArXiv Astrophysics e-prints

- Arfken G. B., Weber H. J., 1995, *Materials and Manufacturing Processes*
- Bartelmann M., 2001, *A&A*, 370, 754
- Bennett C. L., Fixsen D. J., Hinshaw G., Mather J. C., Moseley S. H., Wright E. L., Eplee R. E., Gales J., Hewagama T., Isaacman R. B., Shafer R. A., Turpie K., 1994, *ApJ*, 434, 587
- Bennett C. L., Halpern M., Hinshaw G., et al. 2003, *ApJS*, 148, 1
- Bennett C. L., Hill R. S., Hinshaw G., Nolta M. R., Odegard N., Page L., Spergel D. N., Weiland J. L., Wright E. L., Halpern M., Jarosik N., Kogut A., Limon M., Meyer S. S., Tucker G. S., Wollack E., 2003, *ApJS*, 148, 97
- Bersanelli M., Mandolesi N., 2000, *Astrophysical Letters Communications*, 37, 171
- Birkinshaw M., 1999, *Phys. Rep.*, 310, 98
- Bouchet F. R., Gispert R., 1999, *New Astronomy*, 4, 443
- Bouchet F. R., Prunet S., Sethi S. K., 1999, *MNRAS*, 302, 663
- Cayón L., Sanz J. L., Barreiro R. B., Martínez-González E., Vielva P., Toffolatti L., Silk J., Diego J. M., Argüeso F., 2000, *MNRAS*, 315, 757
- Colberg J. M., White S. D. M., Yoshida N., MacFarland T. J., Jenkins A., Frenk C. S., Pearce F. R., Evrard A. E., Couchman H. M. P., Efstathiou G., Peacock J. A., Thomas P. A., The Virgo Consortium 2000, *MNRAS*, 319, 209
- Cremonese G., Marzari F., Burigana C., Maris M., 2002, *New Astronomy*, 7, 483
- Dame T. M., Hartmann D., Thaddeus P., 1996, *Bulletin of the American Astronomical Society*, 28, 1362
- Dame T. M., Hartmann D., Thaddeus P., 2001, *ApJ*, 547, 792
- Diego J. M., Vielva P., Martínez-González E., Silk J., Sanz J. L., 2002, *MNRAS*, 336, 1351
- Doré O., Teyssier R., Bouchet F. R., Vibert D., Prunet S., 2001, *A&A*, 374, 358
- Finkbeiner D. P., 2003, *ApJS*, 146, 407
- Finkbeiner D. P., Davis M., Schlegel D. J., 1999, *ApJ*, 524, 867
- Finkbeiner D. P., Davis M., Schlegel D. J., 2000, *ApJ*, 544, 81
- Geisbüsch J., Kneissl R., Hobson M., 2004, *ArXiv Astrophysics e-prints*
- Giardino G., Banday A. J., Górski K. M., Bennett K., Jonas J. L., Tauber J., 2002, *A&A*, 387, 82
- Goldin A. B., Kowitt M. S., Cheng E. S., Cottingham D. A., Fixsen D. J., Inman C. A., Meyer S. S., Puchalla J. L., Ruhl J. E., Silverberg R. F., 1997, *ApJL*, 488, L161+
- Griffin M. J., Ade P. A. R., Orton G. S., Robson E. I., Gear W. K., Nolt I. G., Radosstiz J. V., 1986, *Icarus*, 65, 244
- Haslam C. G. T., Klein U., Salter C. J., Stoffel H., Wilson W. E., Cleary M. N., Cooke D. J., Thomasson P., 1981, *A&A*, 100, 209
- Haslam C. G. T., Stoffel H., Salter C. J., Wilson W. E., 1982, *A&A Suppl. Ser.*, 47, 1
- Herranz D., Sanz J. L., et al. 2002a, *MNRAS*, 336, 1057
- Herranz D., Sanz J. L., et al. 2002b, *ApJ*, 580, 610
- Hivon E., Wandelt B. D., Gorski K. M., 1998, in *Evolution of Large-Scale Structure: From Recombination to Garching Cosmic Microwave Background Anisotropy Power Spectrum Statistics for High Precision Cosmology*
- Hobson M. P., Barreiro R. B., Toffolatti L., Lasenby A. N., Sanz J., Jones A. W., Bouchet F. R., 1999, *MNRAS*, 306, 232
- Hobson M. P., Jones A. W., Lasenby A. N., Bouchet F. R., 1998, *MNRAS*, 300, 1
- Jenkins A., Frenk C. S., White S. D. M., Colberg J. M., Cole S., Evrard A. E., Couchman H. M. P., Yoshida N., 2001, *MNRAS*, 321, 372
- Lagache G., 2003, *A&A*, 405, 813
- Lagache G., Puget J. L., 2000, *A&A*, 355, 17
- Lagerros J. S. V., 1996a, *A&A*, 310, 1011
- Lagerros J. S. V., 1996b, *A&A*, 315, 625
- Lagerros J. S. V., 1997, *A&A*, 325, 1226
- Lagerros J. S. V., 1998, *A&A*, 332, 1123
- Lamarre J. M., Puget J. L., Bouchet F., 2003, *New Astronomy Review*, 47, 1017
- Leinert C., Abraham P., Acosta-Pulido J., Lemke D., Siebenmorgen R., 2002, *A&A*, 393, 1073
- Müller T. G., 2001, *Planetary and Space Science*, 49, 787
- Müller T. G., Lagerros J. S. V., 1998, *A&A*, 338, 340
- Müller T. G., Lagerros J. S. V., 1999, *AAS/Division for Planetary Sciences Meeting*, 31, 0
- Müller T. G., Lagerros J. S. V., 2002, *A&A*, 381, 324
- Maino D., Burigana C., Maltoni M., Wandelt B. D., Górski K. M., Malaspina M., Bersanelli M., Mandolesi N., Banday A. J., Hivon E., 1999, *A&A Suppl. Ser.*, 140, 383
- Maino D., Farusi A., Baccigalupi C., Perrotta F., Banday A. J., Bedini L., Burigana C., De Zotti G., Górski K. M., Salerno E., 2002, *MNRAS*, 334, 53
- Mather J. C., Fixsen D. J., Shafer R. A., Mosier C., Wilkinson D. T., 1999, *ApJ*, 512, 511
- Moore P., 2000, *The data book of astronomy. The data book of astronomy*, Bristol: Institute of Physics Publishing (IOPP), 2000, 529 p. ISBN 0750306203
- Natoli P., de Gasperis G., Gheller C., Vittorio N., 2001, *A&A*, 372, 346
- Neugebauer G., Miinch G., Kieffer H., Chase S. C., Miner E., 1971, *AJ*, 76, 719
- Puget J.-L., Abergel A., Bernard J.-P., Boulanger F., Burton W. B., Desert F.-X., Hartmann D., 1996, *A&A*, 308, L5+
- Reach W. T., Morris P., Boulanger F., Okumura K., 2003a, *ArXiv Astrophysics e-prints*
- Reach W. T., Morris P., Boulanger F., Okumura K., 2003b, *Icarus*, 164, 384
- Rephaeli Y., 1995, *ARA&A*, 33, 541
- Sanz J. L., Herranz D., Martínez-González E., 2001, *ApJ*, 552, 484
- Schäfer B. M., Pfrommer C., Bartelmann M., 2004, preprint *astro-ph/040399*
- Schlegel D. J., Finkbeiner D. P., Davis M., 1997, *Bulletin of the American Astronomical Society*, 29, 1354
- Schlegel D. J., Finkbeiner D. P., Davis M., 1998, *ApJ*, 500, 525
- Seljak U., Zaldarriaga M., 1996, *ApJ*, 469, 437
- Sokasian A., Gawiser E., Smoot G. F., 2001, *ApJ*, 562, 88
- Song Y., Cooray A., Knox L., Zaldarriaga M., 2003, *ApJ*, 590, 664
- Spergel D. N., Verde L., Peiris H. V., Komatsu E., Nolta M. R., Bennett C. L., Halpern M., Hinshaw G., Jarosik N., Kogut A., Limon M., Meyer S. S., Page L., Tucker G. S., Weiland J. L., Wollack E., Wright E. L., 2003, *ApJ*, submitted, *astro-ph/0302209*
- Springel V., Hernquist L., 2002, *MNRAS*, 333, 649
- Springel V., Yoshida N., White S. D. M., 2001, *New Astronomy*, 6, 79
- Stolyarov V., Hobson M. P., Ashdown M. A. J., Lasenby A. N., 2002, *MNRAS*, 336, 97
- Sunyaev R. A., Zel'dovich I. B., 1972, *Comments Astrophys. Space Phys.*, 4, 173
- Sunyaev R. A., Zel'dovich I. B., 1980, *ARA&A*, 18, 537
- Tegmark M., de Oliveira-Costa A., 1998, *ApJL*, 500, L83+
- Tegmark M., Efstathiou G., 1996, *MNRAS*, 281, 1297

Toffolatti L., Argueso Gomez F., de Zotti G., Mazzei P., Franceschini A., Danese L., Burigana C., 1998, MNRAS, 297, 117
Valls-Gabaud D., 1998, PASA, 15, 111
Vielva P., Barreiro R. B., Hobson M. P., Martínez-González E., Lasenby A. N., Sanz J. L., Toffolatti L., 2001, MNRAS, 328, 1
Vielva P., Martínez-González E., Cayón L., Diego J. M., Sanz J. L., Toffolatti L., 2001, MNRAS, 326, 181
Villa F., Sandri M., Bersanelli M., Butler R. C., Mandolesi N., Mennella A., Marti-Canales J., Tauber J., 2003, ArXiv Astrophysics e-prints
Wandelt B. D., Górski K. M., 2001, Phys. Rev. D, 63, 123002
White M., Hernquist L., Springel V., 2002, ApJ, 579, 16
White M., Majumdar S., 2003, ArXiv Astrophysics e-prints
Wright E. L., 1976, ApJ, 210, 250
Yvon D., Mayet F., 2004, ArXiv Astrophysics e-prints

This paper has been typeset from a $\text{\TeX}/\text{\LaTeX}$ file prepared by the author.